Politecnico di Torino

Department of Mechanical and Aerospace Engineering

Master degree course in Aerospace Engineering

Academic Year 2022/2023

Aeromechanic design processes optimization

Supervisors:

Prof. Christian Maria Firrone

Ing. Antonio Giuseppe D'Ettole

Ing. Tomek Martin

Candidate

Gianmaria Sartor *s282790*

Abstract

Nowadays the main challenge of the aeronautical industry is to produce more and more efficient aircraft with a lower environmental impact. Indeed, as for the naval and aeronautical sectors, the objectives set in the European Green Deal are [19]:

- reduce emissions by 55% by 2030;
- achieve net-zero emissions by 2050.

For this reason a great effort is focused on producing engines that combine high performance and reliability with an high efficiency. The overall improvement of the engine implies an improvement of its components, including the low pressure turbine.
The development of these components starts from the design and ends with the certification. This process is quite long and all the manual operations performed by users often act as a bottleneck. This thesis work, carried out in collaboration with Avio Aero, has the aim of optimizing some processes that are necessary in the development of a new component.
In particular, some aspects related to the field of modal analysis of bladed disks have been considered:

- having the right mesh order for this kind of analysis;
- optimizing several post processing activities;
- improving the process of test data collection.

During the development of the thesis various commercial software were used, such as Hypermesh, Ansys APDL and Matlab. Besides some business tools were utilized, such as the Spotfire dashboard, the "postpro tool" (which is a matlab code) and the business compute cluster (which strongly reduced the time to permform analyses).
These studies were carried out considering a bladed disk that comes from a European project, ARIAS.
So, the ultimate goals to speed up and improve these processes were reached and quantified.

List of acronyms

LPT,	low pressure turbine
HPT,	high pressure turbine
E_k,	kinetic energy
U,	Potential energy
L_e,	work of extarnal forces
q,	generic degree of freedom
F,	damping function
x_i,	i-th degree of freedom
m_i,	mass of the i-th degree of freedom
k_i,	stiffness of the i-th degree of freedom
c_i,	damping of the i-th degree of freedom
ω,	harmonic pulsation
Ω,	rotation speed
Φ,	real eigenvalue
Θ,	imaginary eigenvalue
h or HI,	harmonic index
ND,	nodal diameter
ϕ or $IBPA$,	inter blade phase angle
EO,	engine order
N,	number of blades of a bladed disk

Contents

Chapter 1

Introduction

1.1 E-TDCs: European Technology Development Clusters

The E-TDCs, European Technology Development Clusters, launched in May 2020, is a network operating into the Research and Innovation Field, with a unique collaborative model in Europe, whose members work together under one single framework agreement which defines financial provisions, IP rules, dissemination and publications.

The E-TDCs include up today 33 parties: 22 Research Institutions, 3 SMEs and 8 GE Affiliates, see fig. 1.1. The Academia, Research Centers and SMEs involved have proven technical and scientific skills, as well as unique experimental assets and expertise in the collaborative Research and Innovation environment. The E-TDCs count 10 different Clusters, consisting of Research Institutions and GE Aviation teams, each of them focused on dedicated disciplines or products of GE Aviation interest, set up taking into consideration the complementarity of knowledge and operating on the basis of an Innovation Plan with the following responsibilities:

- to execute and monitor the Innovation Plan and monitor the international scientific scenario;
- to leverage the complementary knowledge and capability of teams;

- to propose, where necessary, extension of the collaboration to other research teams;
- to promote, where necessary, integration with SMEs;
- to evaluate financing opportunities through participation external funded projects;
- to manage publications and events to disseminate the results obtained;
- to identify, train and involve new talent, including through degree theses, PhD, etc. . . ;
- to develop skills and highly specialized human resources.

Figure 1.1: E-TDCs Network and Clusters.

The network extension and the Clusters progress, results, and ongoing plans are overseen trough a well-established Governance structure, see fig. 1.2, which defines Operating Rhythm and key actors. Just in November 25th it has been held the 2021 edition of the E-TDCs Annual Event: LKD.

Figure 1.2: E-TDCs Governance.

This work of thesis has been done in the Structural Dynamic and Integrity Cluster focused on research activities relates to the Aeromechanics: studies related to HCF (High Cycle Fatigue) problems due to greater vibrational phenomena, and to Flutter Analysis. This discipline has become of great interest from the designers, as it ensures that these high performance engines operate safely.

As this subject is of great complexity, to match industries needs FSI (Fluid-Structure Interaction) is still treated in simplified forms, from decoupled and linearized methods. If when validating a design more accurate and time consuming solutions can be adopted, in the first designing phase is of fundamental importance to have available fast and effective tools to give immediate feedback on aeromechanical behavior and design choices impact.

1.2 The jet engine

At the beginning of the history of aviation, the propulsion system of the airplanes consisted in a reciprocating engine which provided power to a propeller. This was in the first years of the twentieth century. But in the 1930s the jet propulsion system was recognized as the best way to get high velocity. During those years the first aircrafts equipped by jet engine flew and in the following years this technology was improved and applied on a large scale in the aeronautical field up to nowadays.

The jet propulsion is based on the third principle of dynamic, which states that *"To every action there is always opposed an equal reaction"*. Indeed the jet engine accelerate an air flow, generating a force. According to the third low of dynamic there is an equal reaction of this force, which is the thrust (fig. 1.3).

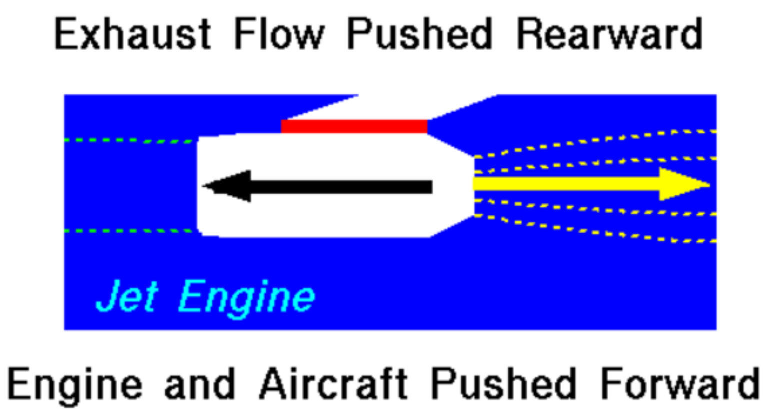

Figure 1.3: Princple of jet propulsion. [22]

The thrust exerted on the engine is proportional to the mass of air expelled by the engine and to the velocity change imparted to it. In other words, the same thrust can be provided either by giving a little acceleration to a large mass of air or a large acceleration to a small mass of air. In practice the former is preferred, since by lowering the jet velocity relative to the atmosphere a higher propulsive efficiency is obtained [1].

1.2.1 Working cycle

So, the jet engine is a heat engine which generates energy using air to provide thrust. The air needs to be accelerated in order to obtain this result. The engine operation is based on the *Brayton-Joule* working cycle. The simplest form of this cycle is based on four phases (fig. 1.4):

- adiabatic compression of the air (1-2)
- combustion of the air with a burning fuel at constant pressure (2-3);
- adiabatic expansion of the hot gases (3-4);
- exhaust of the gases in the atmosphere.

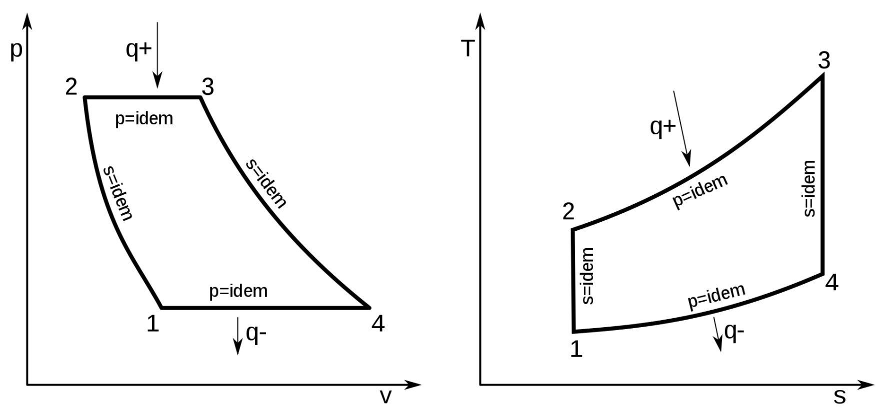

Figure 1.4: The Brayton-Joule working cycle. [23]

In order to perform these phases, each engine is made by the following components (fig. 1.5):

- *air intake*, which is aimed to take air from the environment;
- *compressor*, which compresses the air, bringing it to the optimal pressure for the combustion phase;
- *combustor*, in which the air is mixed with the fuel and is burnt;
- *turbine*, which expands the hot gases coming from the combustor;
- *exhaust system*, which accelerates the gases in order to obtain thrust (only for turbojet and turbofan).

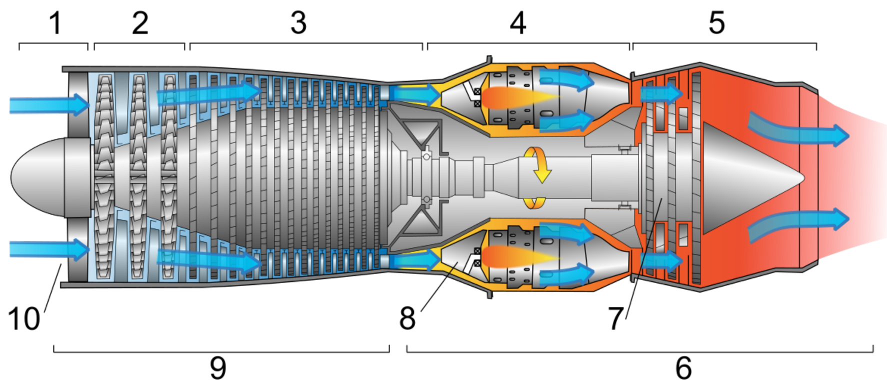

Figure 1.5: Components in a turbo-jet engine. [24]

1.2.2 The aircraft engines

There are basically three thypes of aircraft engine:

- turbojet;
- turboprop;
- turbofan.

The working cycle and the components are basically the same for all of them. There are only few differences.

1.2.2.1 Turbojet

The first aircraft engine was turbojet engine. Nowadays there are not aircraft equipped by this engine, because it is outdated. Nevertheless it is the starting point of the other aircraft engines. It works basically as it has just been explained in the previous section 1.2.

For this engine only a part of the energy of the gases is turned into mechanical power by the turbine, and it is used to drive the compressor. The remainder provides a propulsive jet by accelerating the gases in the nozzle.

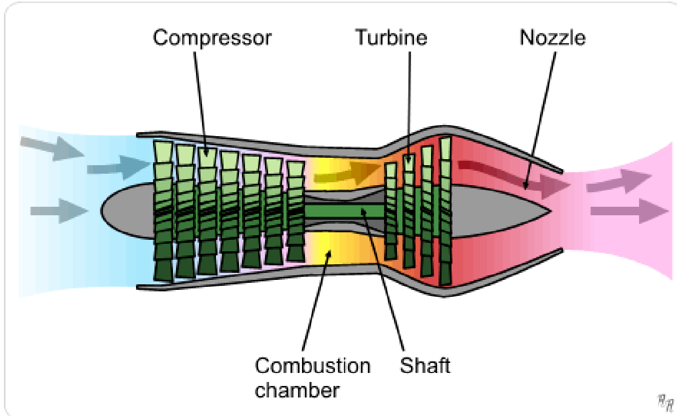

Figure 1.6: Turbojet engine. [25]

1.2.2.2 Turboprop

The turboprop engine is characterized by the presence of an user, which can be a propeller, and by the fact that all the energy is extracted by the turbine to drive the compressor and the user. This engine works better at low speed [1].

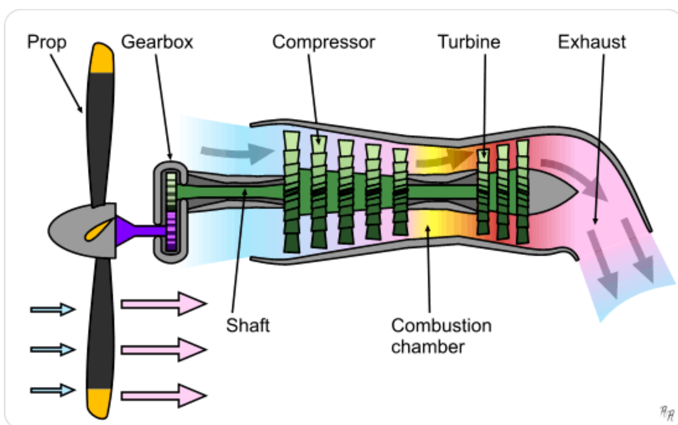

Figure 1.7: Turboprop engine. [26]

1.2.2.3 Turbofan

The turbofan engine is an evolution of the turbojet. This engine is equipped by a fan which takes the air from the enviroment. The peculiar aspect of this engine is the fact

[1] There is another type of engine, very similar to the *turboprop*: the *turboshaft* engine. This engine is equipped in helicopters.

that the air taken by the fan is divided in two flows [2]:

- hot flow, which is processed by the compressor and then is burnt with the fuel;
- cold flow, which passes externally to the hot part of the engine and does not take part to the combustion phase.

The ratio between cold and hot flow is called bypass ratio, and it is an important parameter of turbofan:

$$BPR = \frac{\dot{m}_f}{\dot{m}_c}{}^{3}$$

Usually in these engines the compressor is divided in two part: the low pressure compressor and the high pressure compressor. The compressors are connected by a spool to the relative turbine, so there are the low pressure turbine and the high pressure turbine (fig. 1.8).
So usually the turbofan is composed by two spools which rotates with different angular velocities.

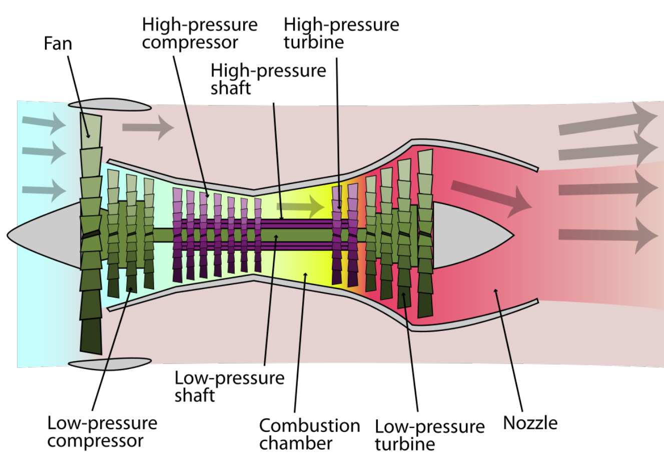

Figure 1.8: Double-spool turbofan engine. [27]

This thesis will be focused on one of all these components of turbofan engine: the

[2]This is done for fuel consumption reasons: in fact, turbofans consume less fuel than turbojets. For this reason nowadays aircrafts are equipped with these engines.

[3]In this equation, *'f'* means *fan* and *'c'* means *core*.

low pressure turbine.

1.3 Low pressure turbine

As explained in the previous chapter, the turbine extracts the kinetic energy of the exapanding gases that comes from the combustion chambers and converts it into shaft power. This power is used to drive compressor (and accessories).
The type of turbine that is used for aircraft engine is the axial-flow turbine. This is composed by several stages and each stage consists in a stator and a rotor (fig. 1.9). In particular:

- *the stator* is the fixed part of the turbine, composed by a set of nozzle guide vanes concentric with the axis of the turbine, which properly direct the airflow in order to obtain the design motion and speed for the rotor;
- *the rotor* is a bladed disk which rotates thanks to the gas flow; this is the part which is connected to the shaft and which contributes (with the rotors of the other stages) to drive the compressor.

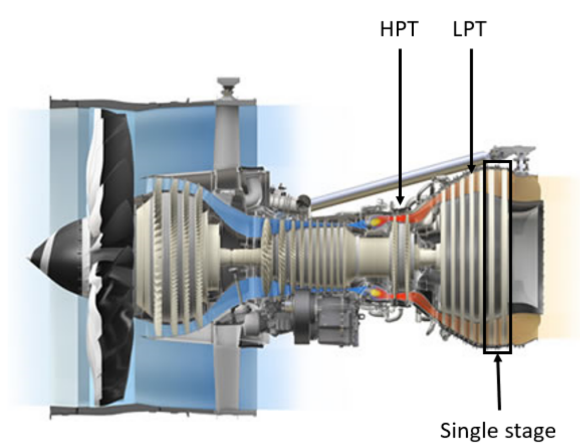

Figure 1.9: Cross section of the *GEnx-1B*. [28]

The nomenclature of a single stage of the turbine is shown in fig. 1.10 (a). It is possible to look at the section of stator vanes and rotor blades and build from it the velocity diagram (fig.1.10 (b)), which represents the magnitude and direction of the gas velocities along the stage.

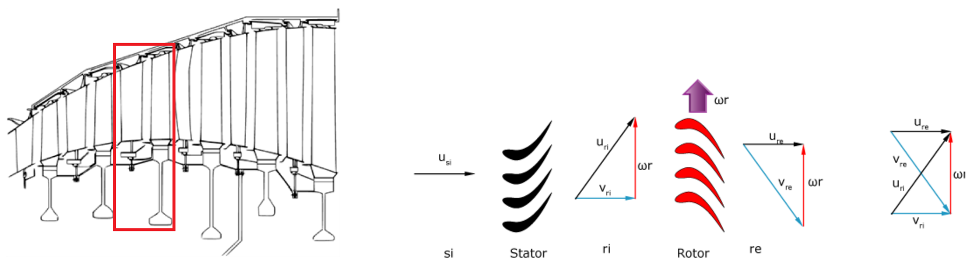

(a) Single turbine stage. [29]　　(b) Velocity diagram. [30]

Figure 1.10: Typical turbine stage and velocity diagram.

As written before, this work will be focused on the low pressure turbine.

1.3.1 Bladed disks

From a theoretical point of view, the rotating components that make up the stages both of axial turbines and axial compressors are considered as a bladed disks, i.e. a disks to which blades are connected, as shown in figure 1.11.

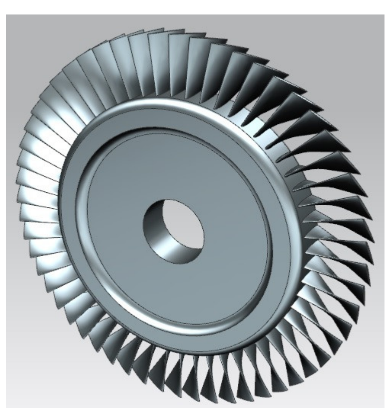

Figure 1.11: Compressor bladed disk. [31]

Bladed disks are composed by a finite number of blades. This number is usually called 'airfoil count'. Each group composed by a single blade with the respective part of the disk is called sector; for studying bladed disks we refer to a single sector, which is called fundamental sector.

So, the fundamental sector is a sector of the bladed disk composed by (fig. 1.12):

- a blade;
- a 'slice' of the disk.

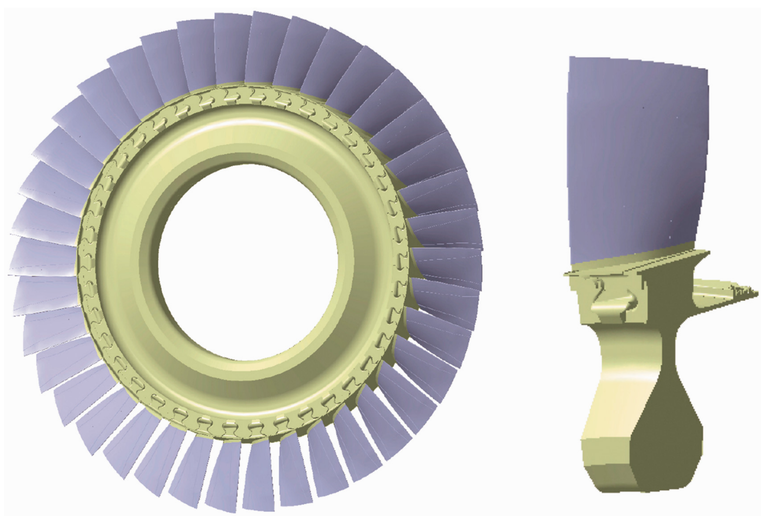

Figure 1.12: Bladed disk (on the left) and the fundamental sector (on the right) of a compressor. [32]

This thesis is focused on the dynamic behavior of these components, which is investigated by performing modal analyses. The study of the dynamic of bladed disks will be explained in the next chapter (chapter 2).

Then in chapter 3 some business processes related to the dynamic analysis of bladed discs will be shown and it will be explained how and by how much they have been optimized.

Chapter 4 will be about the test data collection phase: it will be explained the process to get and to post process the data that comes from experimental tests and the reason

why this is so important.
At the end in chapter 5 there are the conclusions.

1.3.2 Introduction to ARIAS

The bladed disk model that has been used for the studies in this thesis comes from a European project, ARIAS (fig. 1.13).

Figure 1.13: ARIAS project. [44]

ARIAS (Advanced Research Into Aeromechanical Solutions) is a Horizon 2020 funded research project in the field of aeronautical engineering.
The European Union's Horizon 2020 research and innovation program provided financing for this project in the amount of 7.5 million euros as of its debut date on September 1, 2018. *KTH Royal Institute of Technology* is in charge of directing it, and its anticipated duration is four years (48 months).
The ARIAS consortium is composed by leading European universities, research centers and aircraft engine industries, including Avio Aero.
High efficiency (which means creating engines that are more ecologically friendly) and minimal noise are the driving forces behind modern aircraft engine design. Less stages, thinner sections (blades, vanes, seals), and highly loaded components result in

lighter designs. Therefore, these parts are more vulnerable to blade vibrations caused by aerodynamics, which directly jeopardize the machine's structural integrity.
So it is possible to summarize the objectives of this project into three categories:

- to reduce risk of structural failures due to vibrations;
- to optimize engine designs for high efficiency and low noise;
- to reduce design time and costs.

This project is organized in four technical work packages, a work package dedicated to exploitation and communication, and finally a project management. As it is possible to see in figure 1.14, a part of this project is focused on turbines.

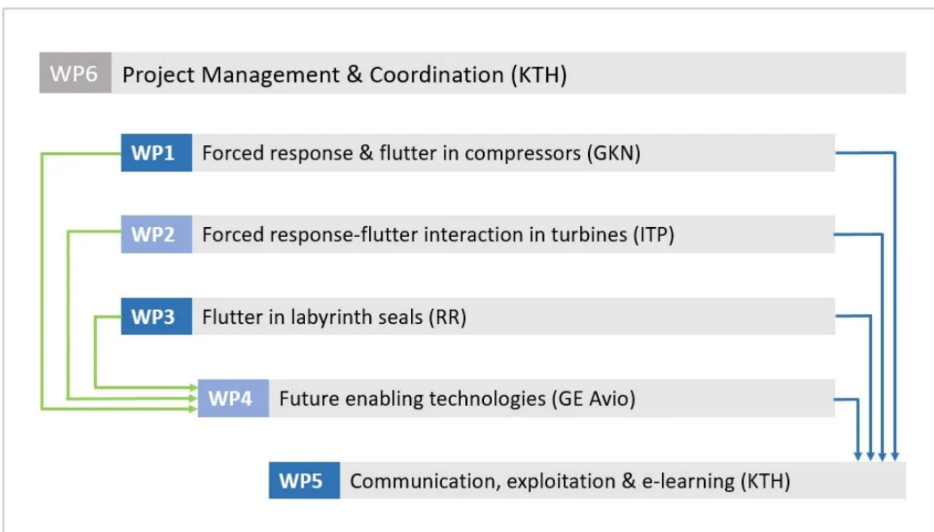

Figure 1.14: ARIAS organization. [45]

Chapter 2

Rotor Dynamics

In the design process of a bladed disk, it is very important to study the time-varying excitation. This is because they are the major responsible of failure due to HCF (High Cycle Fatigue).
Besides, it is important to know the natural frequencies and the modal shapes of the bladed disk related to the operative range of the component.
To understand all these phenomena it is essential to perform modal analyses.

2.1 Modal analysis

The loads that a structure can be subjected can be classified into three categories according to their time-variability:

- static loads, which don't change over time;
- quasi-static loads, which are related to dynamic phenomena but they have similar characteristics to static loads;
- dynamic loads, which changes over time.

The study of structures subjected to time-varying loads is called structural dynamic and the analysis to perform to investigate the dynamic behavior of a structure is the modal analysis.

In order to study the dynamic phenomena, it is necessary to write the equations of motion of the system. For systems with a finite number of degree of freedom (as the one that will be analyzed in this thesis) this can be done by using the Lagrange's equations methods, that is:

$$\frac{d}{dt}\Big(\frac{\partial E_k}{\partial \dot{q}}\Big) + \Big(\frac{\partial U}{\partial q}\Big) = \Big(\frac{\partial L_e}{\partial q}\Big) \tag{2.1}$$

where:

- E_k is the kinetic energy;
- U is the potential energy;
- L_e is the work of external forces;
- q is the generic degree of freedom.

For example, let's consider the system of two degree of freedom $q_1 = x_1$ and $q_2 = x_2$ shown in figure 2.1:

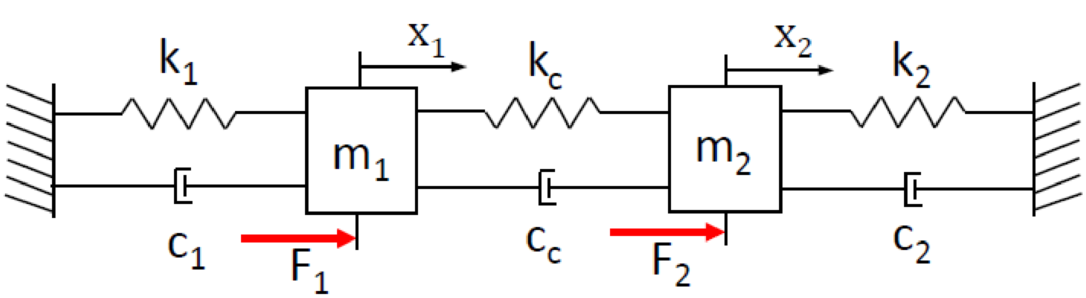

Figure 2.1: Simple system with two degree of freedom. [33]

Since in this case there is also a damping term, another term must be added to the Lagrange equations:

$$\frac{d}{dt}\Big(\frac{\partial E_k}{\partial \dot{q}}\Big) + \Big(\frac{\partial U}{\partial q}\Big) + \Big(\frac{\partial F}{\partial \dot{q}}\Big) = \Big(\frac{\partial L_e}{\partial q}\Big) \tag{2.2}$$

Where F is the damping function.

So, for this example:

- $E_k = \frac{1}{2}m_1\dot{x_1}^2 + \frac{1}{2}m_2\dot{x_2}^2$;
- $U = \frac{1}{2}k_1x_1^2 + \frac{1}{2}k_2x_2^2 + \frac{1}{2}k_c(x_2 - x_1)^2$;
- $F = \frac{1}{2}c_1\dot{x_1}^2 + \frac{1}{2}c_2\dot{x_2}^2 + \frac{1}{2}c_c(\dot{x_2} - \dot{x_1})^2$
- $L_e = F_1x_1 + F_2x_2$
- $\{q\} = \begin{Bmatrix} x_1 \\ x_2 \end{Bmatrix}$

Therefore, deriving:

- kinetic energy

$$\frac{d}{dt}\Big(\frac{\partial E_k}{\partial \dot{x_1}}\Big) = m_1\ddot{x_1} \tag{2.3}$$

$$\frac{d}{dt}\Big(\frac{\partial E_k}{\partial \dot{x_2}}\Big) = m_2\ddot{x_2} \tag{2.4}$$

- potential energy

$$\Big(\frac{\partial U}{\partial x_1}\Big) = k_1x_1 - k_c(x_2 - x_1) \tag{2.5}$$

$$\Big(\frac{\partial U}{\partial x_2}\Big) = k_2x_2 + k_c(x_2 - x_1) \tag{2.6}$$

- damping function

$$\Big(\frac{\partial F}{\partial \dot{x_1}}\Big) = c_1\dot{x_1} - c_c(\dot{x_2} - \dot{x_1}) \tag{2.7}$$

$$\Big(\frac{\partial F}{\partial \dot{x_2}}\Big) = c_2\dot{x_2} + c_c(\dot{x_2} - \dot{x_1}) \tag{2.8}$$

- work of external forces

$$\left(\frac{\partial L_e}{\partial x_1}\right) = F_1 \tag{2.9}$$

$$\left(\frac{\partial L_e}{\partial x_2}\right) = F_2 \tag{2.10}$$

So if we apply the Lagrange's equations method to this system we obtain two equations of motion (in general the number of equation of motion is the same of the number of degree of freedom):

$$m_1\ddot{x}_1 + (c_1 + c_c)\dot{x}_1 - c_c\dot{x}_2 + (k_1 + k_c)x_1 - k_c x_2 = F_1 \tag{2.11}$$

$$m_2\ddot{x}_2 + (c_2 + c_c)\dot{x}_2 - c_c\dot{x}_1 + (k_2 + k_c)x_2 - k_c x_1 = F_2 \tag{2.12}$$

and, in matrix form:

$$\begin{bmatrix} m_1 & 0 \\ 0 & m_2 \end{bmatrix} \begin{Bmatrix} \ddot{x}_1 \\ \ddot{x}_2 \end{Bmatrix} + \begin{bmatrix} c_1 + c_c & -c_c \\ -c_c & c_2 + c_c \end{bmatrix} \begin{Bmatrix} \dot{x}_1 \\ \dot{x}_2 \end{Bmatrix} + \begin{bmatrix} k_1 + k_c & -k_c \\ -k_c & k_2 + k_c \end{bmatrix} \begin{Bmatrix} x_1 \\ x_2 \end{Bmatrix} = \begin{Bmatrix} F_1 \\ F_2 \end{Bmatrix} \tag{2.13}$$

and, more compactly:

$$[M]\{\ddot{x}\} + [C]\{\dot{x}\} + [K]\{x\} = \{F\} \tag{2.14}$$

where:

- $[M]$ is the mass matrix;
- $[C]$ is the damping matrix;
- $[K]$ is the stiffness matrix;
- $\{F\}$ is the external forces vector.

The first step to study the dynamic behavior of a structure is considering only the mass and the stiffness properties of the system. So in the system there is no damping and no external force. This particular case is called study of the free vibrations of the system. So, if we consider the example of fig 2.1, the equations of motion relative to the free vibrations are:

$$[M]\{\ddot{x}\} + [K]\{x\} = 0 \tag{2.15}$$

and so:

$$\begin{bmatrix} m_1 & 0 \\ 0 & m_2 \end{bmatrix} \begin{Bmatrix} \ddot{x_1} \\ \ddot{x_2} \end{Bmatrix} + \begin{bmatrix} k_1 + k_c & -k_c \\ -k_c & k_2 + k_c \end{bmatrix} \begin{Bmatrix} x_1 \\ x_2 \end{Bmatrix} = \begin{Bmatrix} 0 \\ 0 \end{Bmatrix} \tag{2.16}$$

This equation can be solved using the hypothesis of harmonic and stationary vibrations, so that we can write the vector $\{x\}$ as:

$$\{x\} = \{\overline{x}\} e^{i\omega t} \tag{2.17}$$

So that:

$$\{\ddot{x}\} = -\omega^2 \{\ddot{\overline{x}}\} e^{i\omega t} \tag{2.18}$$

And the equations of motion:

$$\begin{bmatrix} -\omega^2 m_1 + k_1 + k_c & -k_c \\ -k_c & -\omega^2 m_2 + k_2 + k_c \end{bmatrix} \begin{Bmatrix} \overline{x_1} \\ \overline{x_2} \end{Bmatrix} = \begin{Bmatrix} 0 \\ 0 \end{Bmatrix} \tag{2.19}$$

This matrix equation has non-trivial solution only if the determinant is equal to zero:

$$det \begin{bmatrix} -\omega^2 m_1 + k_1 + k_c & -k_c \\ -k_c & -\omega^2 m_2 + k_2 + k_c \end{bmatrix} = 0 \tag{2.20}$$

From $det() = 0$ we obtain an equation of second order, from which we obtain two solutions, ω_1 and ω_2.

So this is a eigenvalues (and eigenvectors) problem.

The eigenvalues are the natural pulsations raised to the second power. From eigenvalues we can obtain the respectives eigenvectors, which represent the vibration modes of the system.

That was an easy esample of a system with only two degree of freedom. In case of a system with N degrees of freedom, we have N eigenvalues and N eigenvectors (4.12) and the solution of the problem is a linear combination (4.13) of all the vibration modes:

$$\omega_i^2 \longleftrightarrow \Phi_i \tag{2.21}$$

$$\{x(t)\} = \sum_{i=1}^{N} A_i \{\Phi\}_i \, sin(\omega_i t + \delta_i) \tag{2.22}$$

where the costants A_i and δ_i are obtained by imposing the initial conditions, so they are different depending by the initial status of the system.

The output of the modal analysis are the vibration modes, so both natural frequencies and the relative modes. So this is the reason why the modal analysis is very important.

In the next sections it will be explained how a modal analysis is performed for a complex component as a bladed disk.

2.2 Cyclic symmetry

For the dynamic analysis of bladed disks, as for the other types of structures, it is necessary to start from the modal analysis, in order to recognize natural frequencies and the vibration modes.

The next step is to identify the typical frequencies of the external time-depending loads and then calculate the response of the structure.

These analyses can be performed by exploiting the cyclic symmetry. As written before, the concept that underlies cyclic symmetry is that these components are composed of identical sectors (to a first approximation). This means that the analysis of the entire component is superfluous becuase it is possible to obtain the same results by considering just a single sector.

To better understand the cyclic symmetry, let's consider a single sector of a bladed disk composed by N sectors and then let's model it with a simplified model with two degree of freedom, as shown in fig 2.2.

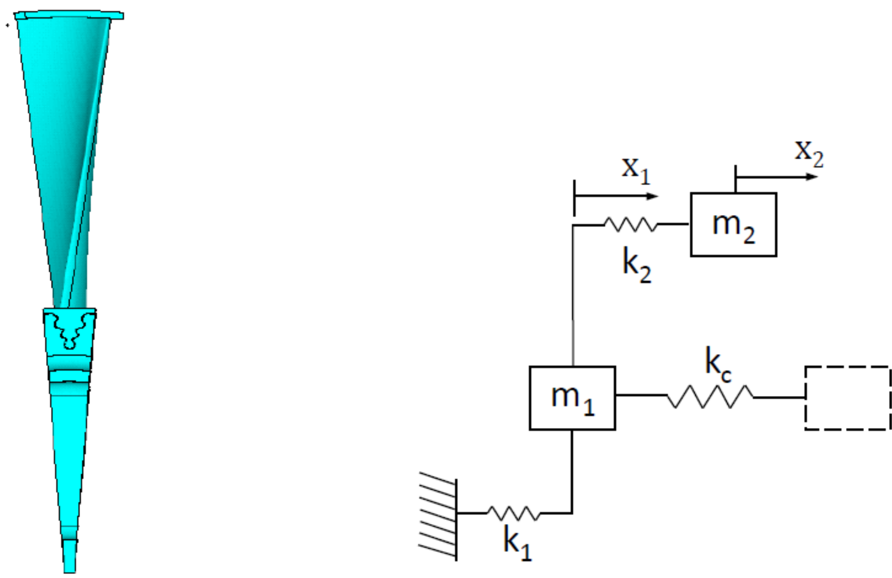

Figure 2.2: Model with two degree of freedom of a single sector. [34]

Considering the adjacent sectors, it is possible to rebuild all the disk (fig 2.3).

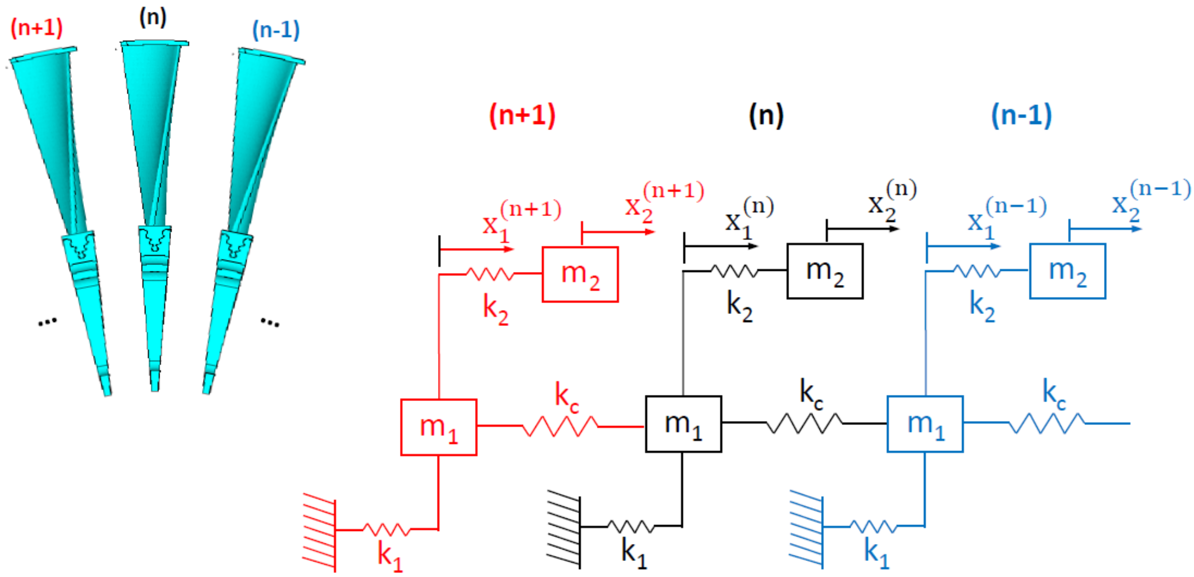

Figure 2.3: Adjacent models. [35]

So, by using the Lagrange's equations methods we obtain the equation of motion of the model, which are two as the number of degree of freedom:

$$m_1\ddot{x}_1{}^{(n)}+k_1x_1{}^{(n)}+k_2(x_1{}^{(n)}-x_2{}^{(n)})+k_c(x_1{}^{(n)}-x_1{}^{(n+1)})+k_c(x_1{}^{(n)}-x_1{}^{(n-1)}) = 0 \quad (2.23)$$

$$m_2\ddot{x}_2{}^{(n)} + k_2(x_2{}^{(n)} - x_1{}^{(n)}) = 0 \quad (2.24)$$

and, in matrix form:

$$\begin{bmatrix} m_1 & 0 \\ 0 & m_2 \end{bmatrix} \begin{Bmatrix} \ddot{x}_1{}^{(n)} \\ \ddot{x}_2{}^{(n)} \end{Bmatrix} + \begin{bmatrix} k_1+k_2+2k_c & -k_2 \\ -k_2 & k_2 \end{bmatrix} \begin{Bmatrix} x_1{}^{(n)} \\ x_2{}^{(n)} \end{Bmatrix} + \\ + \begin{bmatrix} -k_c & 0 \\ 0 & 0 \end{bmatrix} \begin{Bmatrix} x_1{}^{(n+1)} \\ x_2{}^{(n+1)} \end{Bmatrix} + \begin{bmatrix} -k_c & 0 \\ 0 & 0 \end{bmatrix} \begin{Bmatrix} x_1{}^{(n-1)} \\ x_2{}^{(n-1)} \end{Bmatrix} = \begin{Bmatrix} 0 \\ 0 \end{Bmatrix} \quad (2.25)$$

and, more compactly:

$$[m^{(n)}]\left\{\ddot{x}^{(n)}\right\} + [k^{(n)}]\left\{x^{(n)}\right\} + [k_c^{(n)}]\left\{x^{(n+1)}\right\} + [k_c^{(n)}]\left\{x^{(n-1)}\right\} = \{0\} \quad (2.26)$$

So, these are the equation of motion for the generic sector n.

Now, if we write the equation for all the sector (so from the sector 1 to the sector N) we will obtain $2N$ equation:

$$[m^{(1)}]\left\{\ddot{x}^{(1)}\right\} + [k^{(1)}]\left\{x^{(1)}\right\} + [k_c^{(1)}]\left\{x^{(2)}\right\} + [k_c^{(1)}]\left\{x^{(N)}\right\} = \{0\} \tag{2.27}$$

$$[m^{(2)}]\left\{\ddot{x}^{(2)}\right\} + [k^{(2)}]\left\{x^{(2)}\right\} + [k_c^{(2)}]\left\{x^{(3)}\right\} + [k_c^{(2)}]\left\{x^{(1)}\right\} = \{0\} \tag{2.28}$$

$$\ldots$$

$$[m^{(n)}]\left\{\ddot{x}^{(n)}\right\} + [k^{(n)}]\left\{x^{(n)}\right\} + [k_c^{(n)}]\left\{x^{(n+1)}\right\} + [k_c^{(n)}]\left\{x^{(n-1)}\right\} = \{0\} \tag{2.29}$$

$$\ldots$$

$$[m^{(N)}]\left\{\ddot{x}^{(N)}\right\} + [k^{(N)}]\left\{x^{(N)}\right\} + [k_c^{(N)}]\left\{x^{(1)}\right\} + [k_c^{(N)}]\left\{x^{(N-1)}\right\} = \{0\} \tag{2.30}$$

and, more compactly:

$$[M]\left\{\ddot{X}\right\} + [K]\{X\} = \{0\} \tag{2.31}$$

So, by resolving this system of $2N$ equations it is possible to obtain the natural frequencies and vibration modes of the bladed disk. But, as written before, it is possible to simplify this problem thanks to the cyclic symmetry.

Now, let's consider a generic mode Φ:

$$\{\Phi\} = \left\{\begin{array}{c} \Phi^{(1)} \\ \Phi^{(2)} \\ \ldots \\ \Phi^{(n)} \\ \ldots \\ \Phi^{(N-1)} \\ \Phi^{(N)} \end{array}\right\} \tag{2.32}$$

where the generic mode $\Phi^{(n)}$ is associated to the sector n.

Solids with cyclic symmetry have particular modal properties. In fact for these components can exist two type of modes:

- modes associated with a single eigenvalue;
- pairs of modes with the same eigenvalue.

The first ones (associated with a single eigenvalue) can be:

- equal modal shapes in every sector:

$$\Phi^{(n)} = \Phi^{(n+1)} \tag{2.33}$$

- equal modal shapes, but of opposite sign, in every sector:

$$\Phi^{(n)} = -\Phi^{(n+1)} \tag{2.34}$$

The other type of modes are grouped into couples and each couple is associated to a single eigenvalue (i.e. to a single value of natural frequency). So, let's call two eigenvectors with the same eigenvalue $\{\Phi\}$ and $\{\Phi'\}$. In general they are not orthogonal, but if $\{\Phi'\}$ is an eigenvector, it must exists $\left\{\hat{\Phi}\right\}$ so that:

$$\{\Phi'\} = c\,\{\Phi\} + s\left\{\hat{\Phi}\right\} \tag{2.35}$$

It can be demonstrated that $\left\{\hat{\Phi}\right\}$ is orthogonal to $\{\Phi\}$ and it is an eigenvector. Therefore, it can also be demonstrated that if two eigenvector are:

- orthogonal;
- normalized;
- associated to the same eigenvalue;

a linear combination of them is an eigenvector. So:

$$\{\Phi'\} = a\{\Phi\} + b\left\{\hat{\Phi}\right\} \tag{2.36}$$

is an eigenvector. The coefficients a and b are usually real, but in this case we choose to use complex value.

In this way it is possible to obtain complex modes. So:

$$\left\{\overline{\Theta}\right\} = \{\Phi\} + i\left\{\hat{\Phi}\right\} \tag{2.37}$$

where i is $\mid i^2 = -1$.

Now we want ot understand if it is possible to perform a modal analysis for a single sector and then expand the result to the entire bladed disk. So let's consider a complex mode $\left\{\overline{\Theta}\right\} = \{\Phi\} + i\left\{\hat{\Phi}\right\}$:

$$\left\{\overline{\Theta}\right\} = \begin{Bmatrix} \overline{\Theta}^{(1)} \\ \overline{\Theta}^{(2)} \\ \dots \\ \overline{\Theta}^{(n)} \\ \dots \\ \overline{\Theta}^{(N-1)} \\ \overline{\Theta}^{(N)} \end{Bmatrix} \tag{2.38}$$

If we consider $\left\{\overline{\Theta}'\right\} = \{\Phi'\} + i\left\{\hat{\Phi}'\right\}$ obtained through a rigid rotation of an angle ϕ

equal to the width of the sector, this would still be a modal shape of the system:

$$\{\overline{\Theta}\} = \left\{ \begin{array}{c} \overline{\Theta}^{(N)} \\ \overline{\Theta}^{(1)} \\ \dots \\ \overline{\Theta}^{(n-1)} \\ \dots \\ \overline{\Theta}^{(N-2)} \\ \overline{\Theta}^{(N-1)} \end{array} \right\} \tag{2.39}$$

The relation between the two modes is:

$$\{\overline{\Theta}\} = \left\{\overline{\Theta}'\right\} e^{-i\phi} \tag{2.40}$$

And for the generic sector:

$$\left\{\overline{\Theta}^{(n-1)}\right\} = \left\{\overline{\Theta}^{(n)}\right\} e^{-i\phi} \tag{2.41}$$

So, let's discuss the reason why introducing complex modes for bladed disks.

If we consider real modes, all the degrees of freedom of the system vibrate in phase with each other, reaching at the same time the maximum amplitude, the minimum amplitude and also the value of zero amplitude. This does not happen for complex modes.

Let's consider two corresponding points 1 and 2 which belong to two adjacent sectors. The point 2 vibrates with a phase shift ϕ with respect to 1. So in general for all the corresponding points on the N identical sectors that build up the bladed disk, the dynamics described by a complex mode is a rotating wave, characterized by a phase shift equal to ϕ between adjacent sectors.

2.2.1 Harmonic index

Now we need to understand the admittable angles for ϕ. If we consider a bladed disk made by N sectors, after N rotations of the eigenvector of the first sector we need to obtain again the same eigenvector. So, after N rotations of ϕ we need to obtain an angle equal to an integer multiple of 360 (or 2π):

$$N\phi = 2\pi h \rightarrow \phi = \frac{2\pi h}{N} \tag{2.42}$$

where:

- ϕ is called **inter-blade phase angle**;
- h is called **harmonic index** and it is an integer.

So, considering the relation:

$$\left\{\overline{\Theta}^{(n)}\right\} = \left\{\overline{\Theta}^{(n-1)}\right\} e^{i\phi} \rightarrow \left\{\overline{\Theta}^{(n)}\right\} = \left\{\overline{\Theta}^{(n-1)}\right\} e^{ih\frac{2\pi}{N}} \tag{2.43}$$

- for $\phi = 0 \rightarrow h = 0$ we obtain equal mode shapes in every sector:

$$\overline{\Theta}^{(n)} = \overline{\Theta}^{(n-1)} \tag{2.44}$$

- for $\phi = \pi \rightarrow h = N/2$ we obtain equal mode shapes, but of opposite sign, in every sector:

$$\overline{\Theta}^{(n)} = -\overline{\Theta}^{(n-1)} \tag{2.45}$$

  This mode exists only if the number of sectors N is even.

  This first two modes ($h = 0$ and $h = N/2$) are real.

- for all the other values of ϕ (and the related h) the modes are all complex, so they describe a rotating wave , characterized by a phase shift equal to ϕ between adjacent sectors.

$$\left\{\overline{\Theta}^{(n)}\right\} = \left\{\overline{\Theta}^{(n-1)}\right\} e^{ih\frac{2\pi}{N}} \tag{2.46}$$

Given the periodicity of the function e^{ix} it is possible to consider only the harmonic indices:

- $h = 0, 1, 2, ..., \frac{N}{2} - 1, \frac{N}{2}$ for bladed disks with a even number of sectors;
- $h = 0, 1, 2, ..., \frac{N-1}{2} - 1, \frac{N-1}{2}$ for bladed disks with a odd number of sectors.

It can be demonstrated that the harmonic index h indicates the number of diametrical lines with zero displacement, called *nodal diameters*. In the following figure 2.4 the nodal diameters for different modes of a bladed disk composed by $N = 40$ sectors are shown in black.

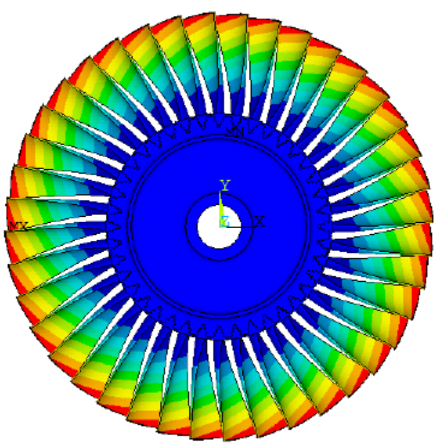

(a) ND=0 [47]

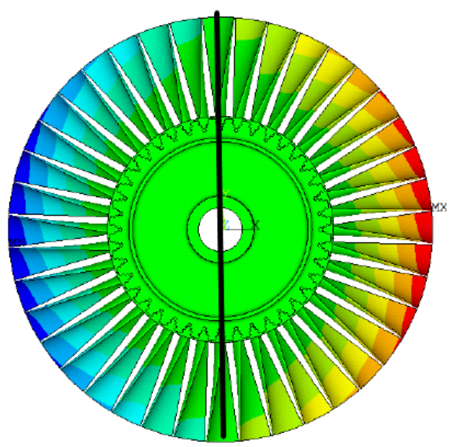

(b) ND=1 [48]

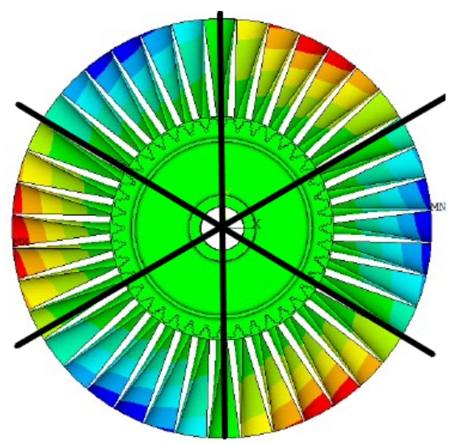

(c) ND=3 [49]

Figure 2.4: Graphical explanation of nodal diameters.

Thanks to the complex modes and harmonic indices it is possible to perform a modal analysis for a single sector and expand the solution for all the bladed disk.
In the next section will be explained how to perform this with the simple model composed by two degree of freedom.

2.3 Modal analysis with cyclic symmetry

So, let's consider the equation of motion that we obtained before for the model in fig 2.2:

$$m_1\ddot{x_1}^{(n)}+k_1 x_1{}^{(n)}+k_2(x_1{}^{(n)}-x_2{}^{(n)})+k_c(x_1{}^{(n)}-x_1{}^{(n+1)})+k_c(x_1{}^{(n)}-x_1{}^{(n-1)})=0 \tag{2.47}$$

$$m_2\ddot{x_2}^{(n)}+k_2(x_2{}^{(n)}-x_1{}^{(n)})=0 \tag{2.48}$$

As written in the first section, for the modal analysis we use the hypothesis of harmonic vibrations:

$$\left\{x^{(n)}\right\}=\left\{\overline{x}^{(n)}\right\}e^{i\omega t} \tag{2.49}$$

So:

$$-\omega^2 m_1\overline{x}_1^{(n)}+k_1\overline{x}_1^{(n)}+k_2(\overline{x}_1^{(n)}-\overline{x}_2^{(n)})+k_c(\overline{x}_1^{(n)}-\overline{x}_1^{(n+1)})+k_c(\overline{x}_1^{(n)}-\overline{x}_1^{(n-1)})=0 \tag{2.50}$$

$$-\omega^2 m_2\overline{x}_2^{(n)}+k_2(\overline{x}_2^{(n)}-\overline{x}_1^{(n)})=0 \tag{2.51}$$

Now we can use the relation of the cyclic symmetry:

$$\left\{\overline{\Theta}^{(n)}\right\}=\left\{\overline{\Theta}^{(n-1)}\right\}e^{ih\frac{2\pi}{N}} \tag{2.52}$$

That, in this case becomes:

$$\overline{x}_1^{(n)}=\overline{x}_1^{(n-1)}e^{ih\frac{2\pi}{N}} \rightarrow \overline{x}_1^{(n-1)}=\overline{x}_1^{(n)}e^{-ih\frac{2\pi}{N}} \tag{2.53}$$

$$\overline{x}_1^{(n+1)}=\overline{x}_1^{(n)}e^{ih\frac{2\pi}{N}} \tag{2.54}$$

Then the equations of motion become:

$$-\omega^2 m_1\overline{x}_1^{(n)}+k_1\overline{x}_1^{(n)}+k_2(\overline{x}_1^{(n)}-\overline{x}_2^{(n)})+k_c(\overline{x}_1^{(n)}-\overline{x}_1^{(n)}e^{ih\frac{2\pi}{N}})+k_c(\overline{x}_1^{(n)}-\overline{x}_1^{(n)}e^{-ih\frac{2\pi}{N}})=0 \tag{2.55}$$

$$-\omega^2 m_2\overline{x}_2^{(n)}+k_2(\overline{x}_2^{(n)}-\overline{x}_1^{(n)})=0 \tag{2.56}$$

And in matrix form:

$$\left(-\omega^2\begin{bmatrix} m_1 & 0 \\ 0 & m_2 \end{bmatrix} + \begin{bmatrix} k_1+k_2+2k_c-k_c e^{ih\frac{2\pi}{N}}-k_c e^{-ih\frac{2\pi}{N}} & -k_2 \\ -k_2 & k_2 \end{bmatrix}\right)\begin{Bmatrix} \overline{x_1}^{(n)} \\ \overline{x_2^{(n)}} \end{Bmatrix} = \begin{Bmatrix} 0 \\ 0 \end{Bmatrix} \tag{2.57}$$

We obtain a system in which the mass matrix and the stiffness matrix depend on the harmonic index h. So it is possible to obtain natural frequencies and modal shapes for the complete system by solving this simple system (related to a single sector) as the value of h varies.

That was a simple example of a system with two degree of freedom, but it is valid also for system with a lot of degree of freedom, as the one that will be analyzed in this thesis.

2.3.1 FreND diagram

As outputs of the modal analysis, other than the values of natural frequencies and the recognition of modal shapes, it could be useful to plot the *FreND* diagram. This diagram has in the x-axis the nodal diameter (whichis equal to the harmonic index) and in the y-axis the frequency (in fact ***FreND*** $\rightarrow$ **Fre**quency vs **N**odal **D**iameter). It describes how the value of the natural frequency of a mode shape changes with respect with the nodal diameter.

By this plot it is possible to note that as nodal diameter grows, there is an initial increase of the natural frequencies. But then, for higher nodal diameters, that value aims to a horizontal asymptote. This particular behavior is more evident for high values of natural frequencies. The reason why this happens is contained in the definition of nodal diameter: indeed, as explained before, the nodal diameter is the number of lines with zero displacement. So the higher is the nodal diameter value, the greater is the stiffness of the structure and so also the natural frequencies will be greater.

In some cases there could be a veering zone in this diagram. The veering is a region where two modal families interchange mode shapes, showing a crossing of the natural frequencies.
In the figure 2.5 it is shown an example of a FreND diagram.

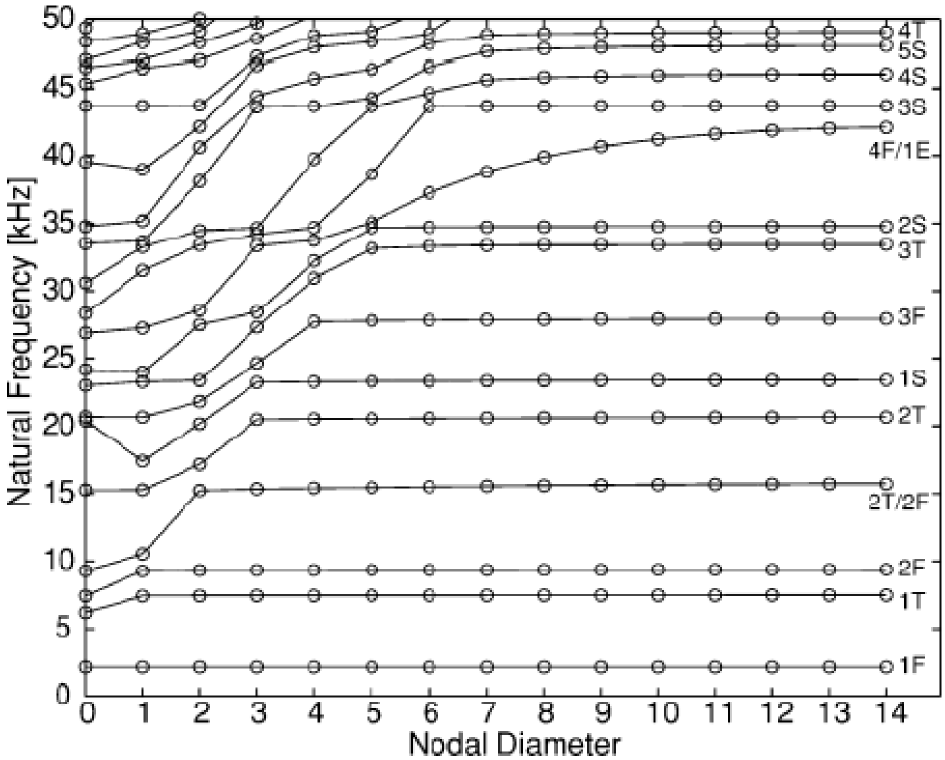

Figure 2.5: Example of FreND diagram. [36]

2.4 Forced response

After having identified the typical frequencies of the forces, it will be necessary to verify the presence of resonances within the operating range of the machine and calculate the amplitude of the response.
First of all it is important to know the loads that a low pressure turbine (which is the object of this thesis) is subjected during its operational life. These can be divided into four categories:

- Pressure loads, caused by the different pressure field between suction side and pressure side of the LPT; this different distribuition of pressure combined with the presence of blades causes the rotation of the turbine, which is necessary to drive the compressor;

- Inertial loads, caused by the high angular velocity of the turbine, which generates centrifugal forces in the external blades;

- Thermal loads, caused by the hot gases which come from the combustion chamber and which expand in the turbine, implying thermal gradients;

- Pre-Twist loads caused by the pre-load to whom the blades are subjected when they are installed; this pre-load is necessary to obtain the correct positioning of the airfoil with respect to the flux during operation.

Let's focus on time-depending loads in a LPT. Usually they can be originated from different sources:

- the pressure field, which induces vibrations whose frequency is a multiple of the angular velocity of the turbine. In this case the excitation are called *synchronous vibrations*

- flux instability, rotor stall or others, which induce vibrations whose frequency is not linked to the angular velocity of the turbine. For this reason this excitation are called *non-synchronous vibrations*.

We will take into account *synchronous vibrations*. Let's consider the angular velocity of the LPT Ω constant. The dynamic loads which cause synchronous vibrations can be described by using the Fourier series as function of the angle $\alpha = \Omega t$ as:

$$F(\alpha) = F_0 + \sum_{EO} F^{(EO)} cos(EO\alpha + \delta) \tag{2.58}$$

The generic component EO of the harmonic force is identified by a parameter called ***Engine Order***, which is defined as:

$$EO = \frac{\omega}{\Omega} \tag{2.59}$$

So it can be written as:

$$F^{(n)} = F^{(EO)} cos(\omega t + \delta) \tag{2.60}$$

The study of the forced response consists in understanding if exciting loads can represent dangerous conditions for the turbine. These conditions are called resonance condition, and correspond to the cases in which the pulsation of the exciting load coincides with one of the natural frequencies of the system.

Now, to understand if an exciting load can represent a resonance condition it is useful to use a graphical tool, which is called *Campbell diagram*. In this diagram there is rotation speed on x-axis and frequency on y-axis.

So, if we do not consider the effects of the temperature and of the centrifugal loads, the natural frequencies are represented as a set of line parallel to the x axis. But actually the value of natural frequencies vary because of these two effects; so, more correctly, they are lines whose trend depends on the rotation speed.

Instead the excitation frequencies are represented by lines which start from axis origin and the EO indicates the slope of these lines; indeed:

$$\omega = EO\Omega \tag{2.61}$$

In the figure 2.6 it is shown an example of a Campbell diagram.

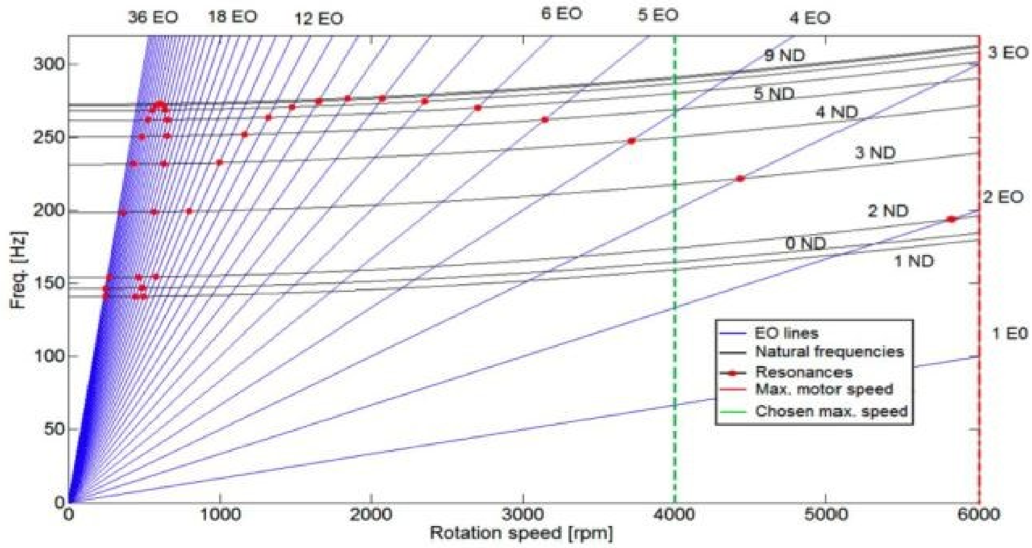

Figure 2.6: Example of Campbell diagram. [37]

Potential resonance situations are represented by the crossings between excitants' curves and the natural frequencies lines. But crossing is a necessary but not sufficient condition to resonance.

Let's consider a crossing. If we consider the the harmonic index h related to the natural frequency, it can be demonstrated that the crossing represents a resonance condition only if:

$$h = EO \tag{2.62}$$

So, only if the value of the harmonic index is equal to the value of the EO of the load, the crossing represents a resonance condition.

As written before, the harmonic index h can assume the following values:

$$0 \leq h \leq N - 1 \tag{2.63}$$

where N is the number of sector of the bladed disk.

However, as for the forcings, the EO value can be greater than $N - 1$. It can be demonstrated that for:

$$EO \geq N - 1 \tag{2.64}$$

the resonance conditions are represented by:

$$EO - kN = h \tag{2.65}$$

where $k = 0, 1, 2, 3, ...$, depending on the value of the EO.

So, in order to understand for which value of h an EO can cause resonance, it is used a particular diagram, called the *Zig Zag diagram*. In this diagram there is the harmonic index h on x-axis and the EO on y-axis. The name of this diagram derives from the form that it takes, since (as explained in section 4.2) it is sufficient to consider the following values of h:

- $0 \leq h \leq \frac{N}{2}$ if N is even;
- $0 \leq h \leq \frac{N-1}{2}$ if N is odd.

In the figures 2.7a and 2.7b are shown two example of *Zig Zag diagram*.

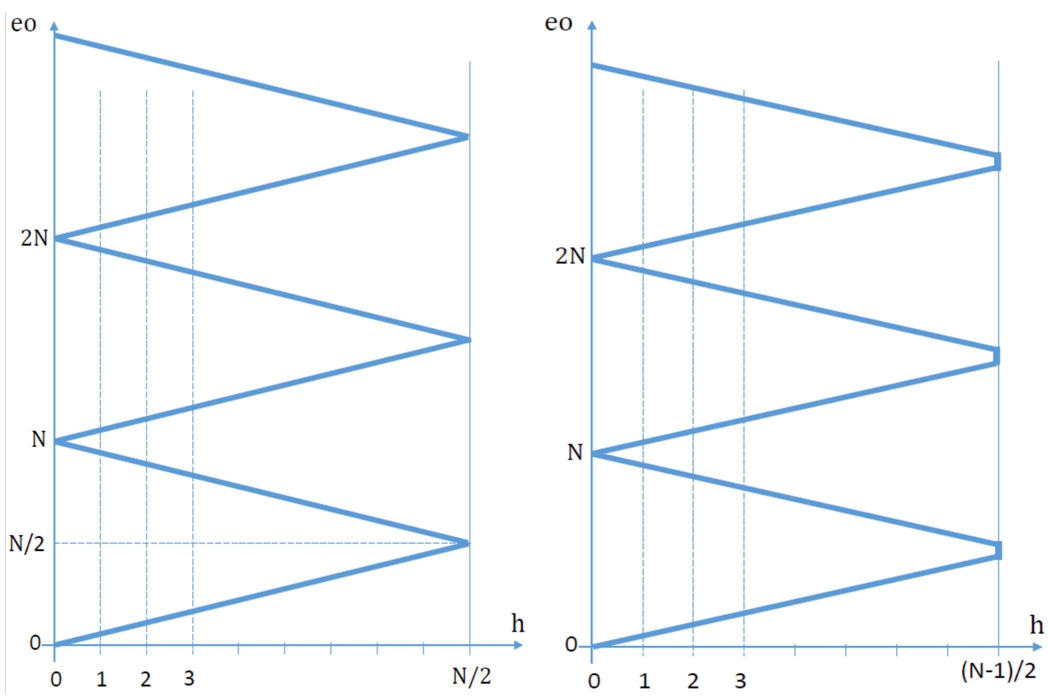

(a) *Zig Zag diagram* if N is even. [38]

(b) *Zig Zag diagram* if N is odd. [39]

Figure 2.7: Types of *Zig Zag diagram*.

2.5 Aeromechanics instabilities

Aeromechanical instabilities must be taken into account when looking at a turbine rotor.

One of the most significant of these is flutter, which occurs when the fluid intensifies the vibration following the initial displacement of the structure.

Aeroelasticity is a field of study that is focused on the relationship between the modal behaviour of a structure and fluid flow. According to the Collar triangle (fig. 2.8), this interaction occurs between three separate fields.

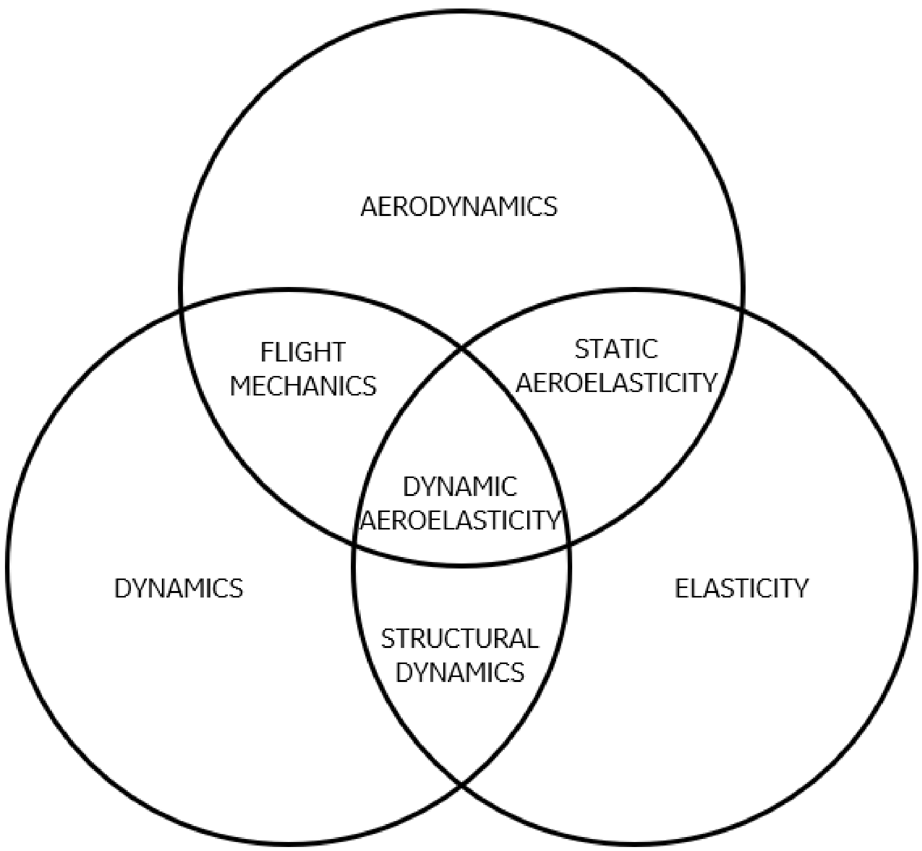

Figure 2.8: Collar triangle.

The three macro areas that compose Collar triangle are:

- aerodynamics:
- dynamics;
- elasticity.

By intersecting these three disciplines we obtain:

- structural dynamics:
- flight mechanics;
- static aeroelasticity, for which only aerodynamic and elastic forces are considered;
- dynamic aeroelasticity, that also include inertial forces.

2.5.1 Classic flutter

The most significant phenomenon associated with dynamic aeroelasticity is flutter. Generally, this problem is studied in the design phase of aircraft wings.
Flutter is brought on by asynchronous vibrations (unlike vibrations due to a forced response, which are strictly related to the EO as seen in the previous section).
When it happens, aerodynamic forces cause the system to become excited, which in turn causes the self excitation of the structure.
To better understand this phenomenon, reference is made to a simplified two-degree-of-freedom model of an aerodynamic profile. This model is represented in the following figure 2.9.

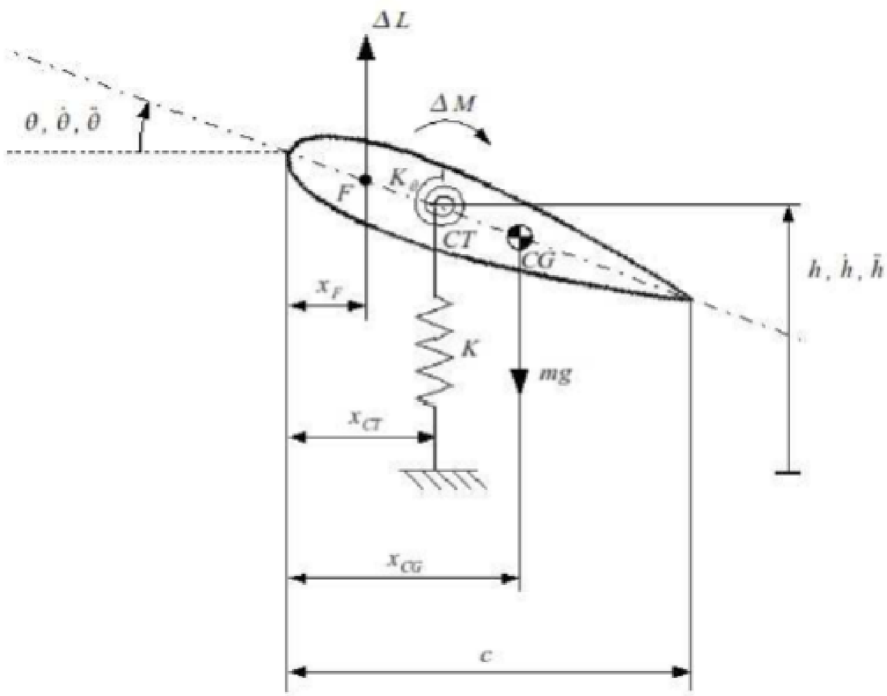

Figure 2.9: Simplified model for flutter. [40]

Where:

- **F** is the aerodynamic center;
- **CT** is the shear center;
- **CG** is the center of gravity;
- K_h is the bending stiffness;
- K_θ is the torsional stiffness.
- ΔL is the lift force and ΔM is the aerodynamic momentum;
- h and θ are the two degree of freedom.

So if we call:

$$\{x\} = \begin{Bmatrix} h \\ \theta \end{Bmatrix} \tag{2.66}$$

the vector with the two degree od freedom, we can express the aerodynamic forces:

$$\{F_a(t)\} = \begin{Bmatrix} \Delta L \\ \Delta M \end{Bmatrix} \tag{2.67}$$

as:

$$\{F_a(t)\} = M_a\{\ddot{x}\} + C_a\{\dot{x}\} + K_a\{x\} \tag{2.68}$$

Where

- M_a is the aerodynamic mass matrix;
- C_a is the aerodynamic damping matrix;
- K_a is the aerodynamic stiffness matrix;

As seen before, the equation of motion of the system of figure 2.9 can be written as:

$$M\{\ddot{x}\} + C\{\dot{x}\} + K\{x\} = \{F\} \tag{2.69}$$

In this case $\{F\}$ is:

$$\{F\} = \{F_e(t)\} + \{F_a(t)\} \tag{2.70}$$

Where $\{F_e(t)\}$ and $\{F_a(t)\}$ represents respectively the external forces and the aerodynamic forces. So:

$$M\{\ddot{x}\} + C\{\dot{x}\} + K\{x\} = \{F_e(t)\} + \{F_a(t)\} \tag{2.71}$$

if we neglect the term of the external forcings we get:

$$M\{\ddot{x}\} + C\{\dot{x}\} + K\{x\} = \{F_a(t)\} \tag{2.72}$$

So if we replace the term $\{F_a(t)\}$ with the equation (4.68) we obtain:

$$(M - M_a)\{\ddot{x}\} + (C - C_a)\{\dot{x}\} + (K - K_a)\{x\} = 0 \tag{2.73}$$

The generic solution of this equation is:

$$\{x(t)\} = \{\overline{x}\}e^{\lambda t} \tag{2.74}$$

where λ is the complex eigenvalue:

$$\lambda = \lambda_r + i\lambda_i \tag{2.75}$$

where the imaginary part represents the frequency of the system while the real part represents its stability. Indeed:

- if $\lambda_r > 0$ the system is unstable;
- if $\lambda_r = 0$ the system is perfectly oscillatory;
- if $\lambda_r < 0$ the system exhibits an exponential decline and so is stable.

λ_r is alled aerodynamic damping coefficent.
Since λ_r is related to $V_{flutter}$, the flutter velocity can be calculated from this value and this will represent a threshold not to be exceeded to avoid this phenomenon.

2.5.2 Flutter in turbomachines

The same factors that were taken into account for the single airfoil profile in the preceding section can be applied to the entire rotor flow while taking the coupling of disturbances between blades into account.
A perturbation on one a blade will not only alter the flow conditions around it. Indeed, due to the aerodynamic coupling [11], it will also move around the rotor and impact the nearby blades (fig 2.10).

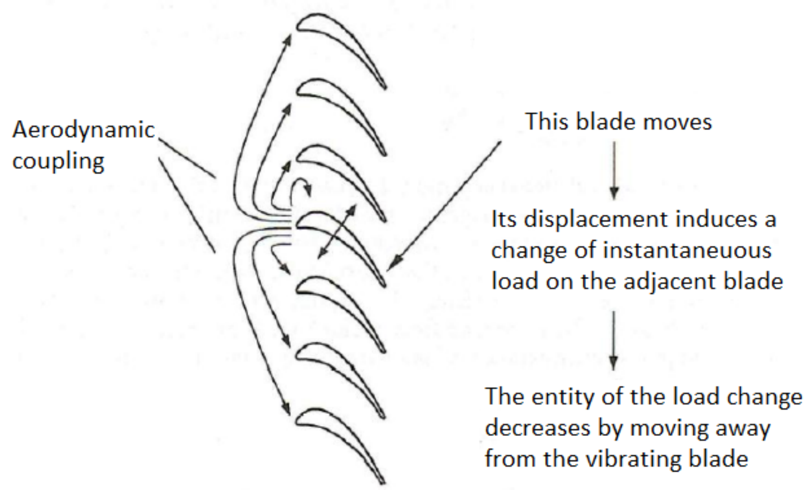

Figure 2.10: Aerodynamic coupling. [41]

Twenty characteristics were identified by A.V. Srinivasan [21] as having the potential to affect the aeroelastic vibrations of bladed discs. The crucial ones are:

- inlet and outlet conditions: pressure and temperature have an impact on aerodynamic damping;
- shock waves, which have a significant impact on the pressure load at the leading edge of the blade;
- tip shroud, which modifies the equation of motion for the system by adding a certain damping;
- Reduced frequency, defined as:

$$k = \frac{c\omega}{2V} \tag{2.76}$$

  The flow is considered as quasi-static when the reduced frequency k is low, whereas it is considered as unstable for high values of k;
- Mistuning[1];

[1] Mistuning is the difference in mass and/or stiffness between sectors of a bladed disk.

- IBPA.

It is essential to understand how blades interact from both an aerodynamic and a structural point of view in order to examine the flutter stability. Even though the precise procedure will not be described in this thesis, the approach nonetheless necessitates an understanding of blade displacements. So, it is necessary to do a prior modal analysis on the assumption that the effect of gas flow on natural frequencies and mode-shapes can be ignored.

As mentioned above, the aerodynamic damping coefficient λ_r can be used to detect flutter instability.

It is feasible to see that the aerodynamic damping is constant with regard to the IBPA when only one oscillating blade is taken into account. Instead, when more blades are taken into account, flutter instability is affected by the IBPA value and exhibits a sinusoidal trend. Additionally, the influence is decreased the further away the blades are from the reference one (fig. 2.11).

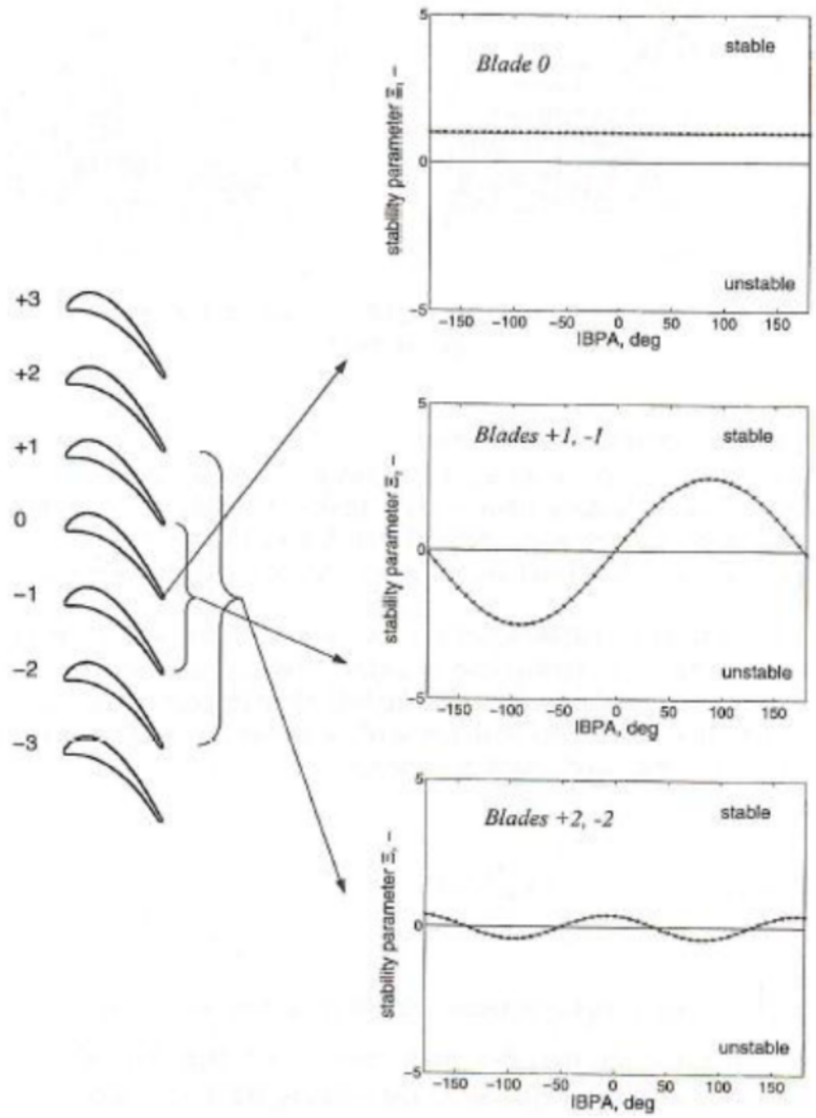

Figure 2.11: Dependence of aerodynamic coupling on the IBPA. [42]

The S-curve, also known as the Aeroplot (shown in figure 2.12), is a typical representation of the aerodynamic damping coefficient variation vs the IBPA assuming to use the superposition principle. The plot makes it possible to distinguish between flutter instability conditions that arise when aerodamping is negative and flutter stability conditions that arise when aerodamping is positive.

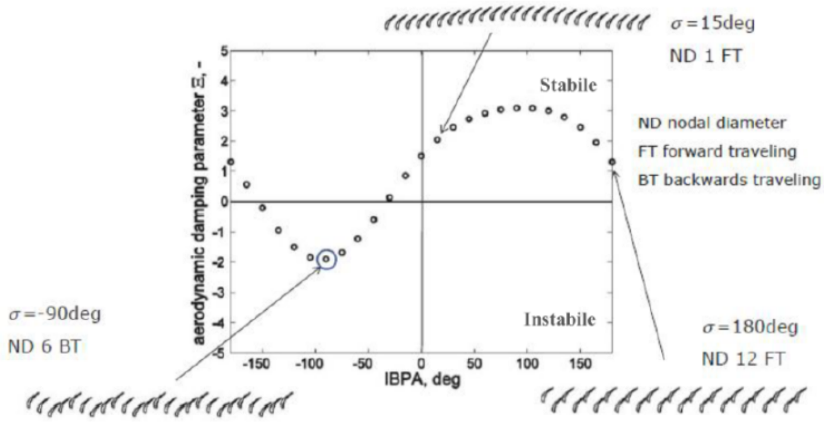

Figure 2.12: Example of aeroplot. [43]

It is very important to study flutter in turbomachines beacuse it can be a cause of failure. An example of bladed disk that has broken due to this phenomenon is shown fin figure 2.13.

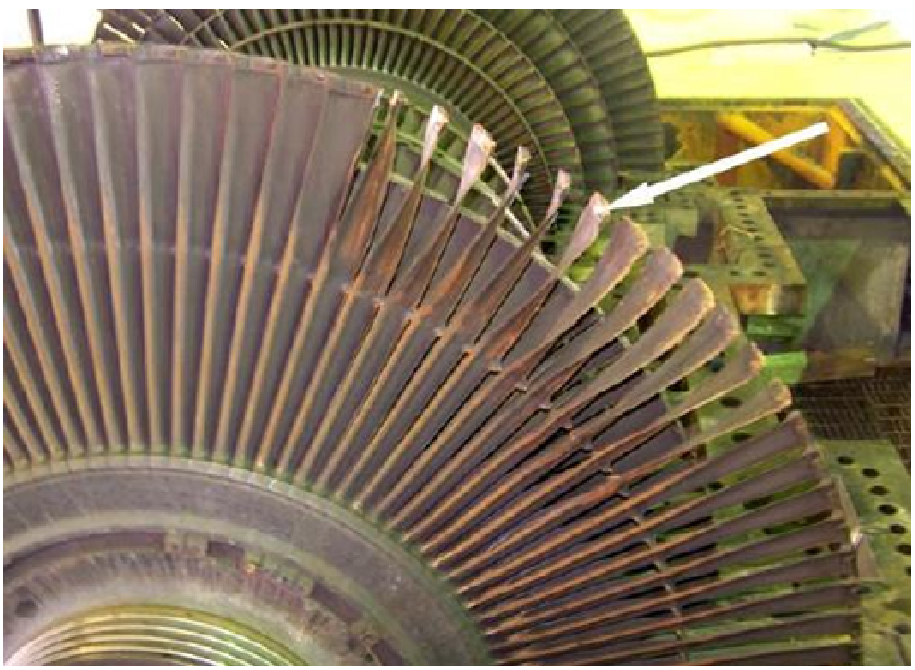

Figure 2.13: Example of failure of a bladed disk due to flutter. [44]

Chapter 3

Optimization of post processing activities related to modal analysis

The model that has been used in this thesis comes from a European project, ARIAS (see section 1.3.2). The ARIAS bladed disk has been analyzed for the modal analysis and for the main part of this thesis.
In the first section of this chapter an overview about the workflow for the study of a bladed disk will be done. Then, in the other sections the modal analysis and the post processing done with this bladed disk will be explained.

3.1 Workflow

In Avio Aero the workflow followed in the design process of a bladed disk is illustrated in figure 3.1.
As written before, this thesis is focused on the modal analysis and in the post processing of it. Referring to the figure 3.1, the aspects taken into account are:

- 3D mesh of the Arias bladed disk;

- modal analysis of the model;
- post processing.

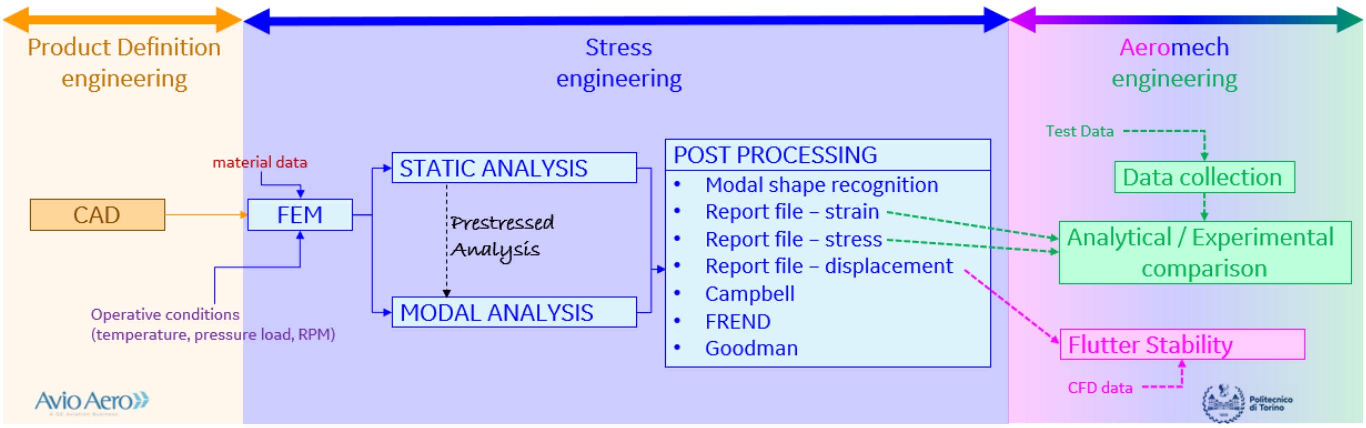

Figure 3.1: Workflow for the study of a bladed disk.

In particular, as for the post processing phase:

- generation of postpro diagrams, i.e.: FreND;
- modal shape recognition;
- generation of report file;

3.2 Meshing of the model

Firstly it has been taken into account the CAD model of ARIAS bladed disk. This model doesn't represent all the disk but only a single sector, for the reasons explained in the the previous chapter. The total amount of sectors for this bladed disk is:

$$N = 146$$

This model has been imported in *Hypermesh*[1] (fig. 3.2(a),(b)). This software has been used to prepare the FE[2] model.

[1] *Altair Hypermesh* is a pre-processing software for high-fidelity finite element modeling [18].

[2] FE means Finite Element

The mesh of the model is a 3D mesh, so it was done by using 3D elements.

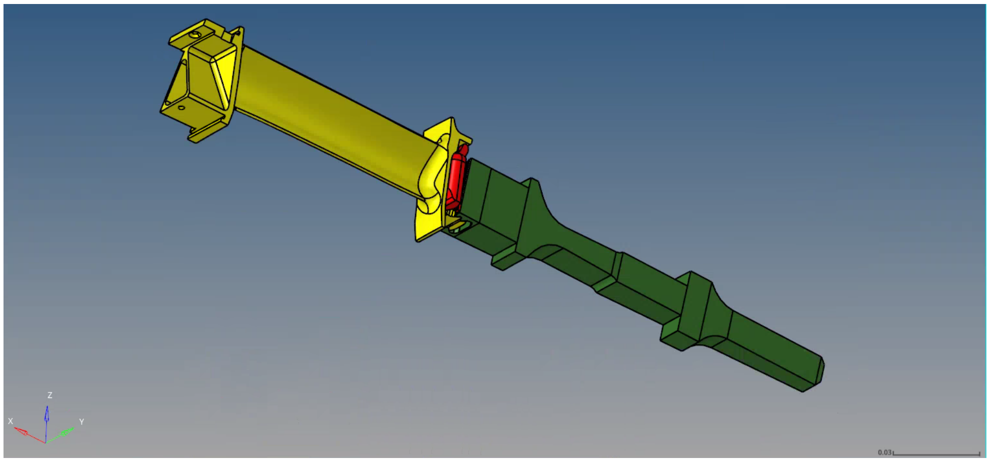

(a)

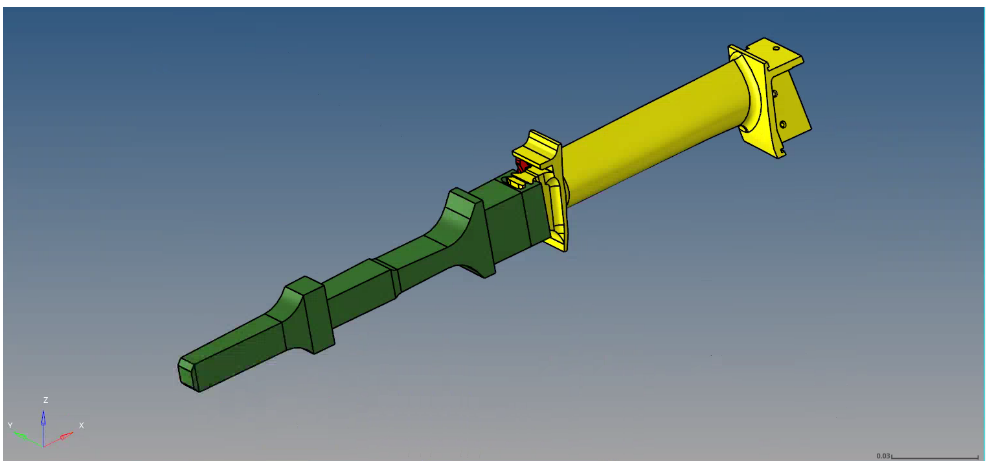

(b)

Figure 3.2: CAD model.

The geometry was composed by:

- disk (fig 3.3);
- blade (fig 3.4);
- damper [3] (fig 3.5);

[3] The damper is a component that is positioned at the base of the blade which dampens the vibrations of the blade itself. In this case it was neglected.

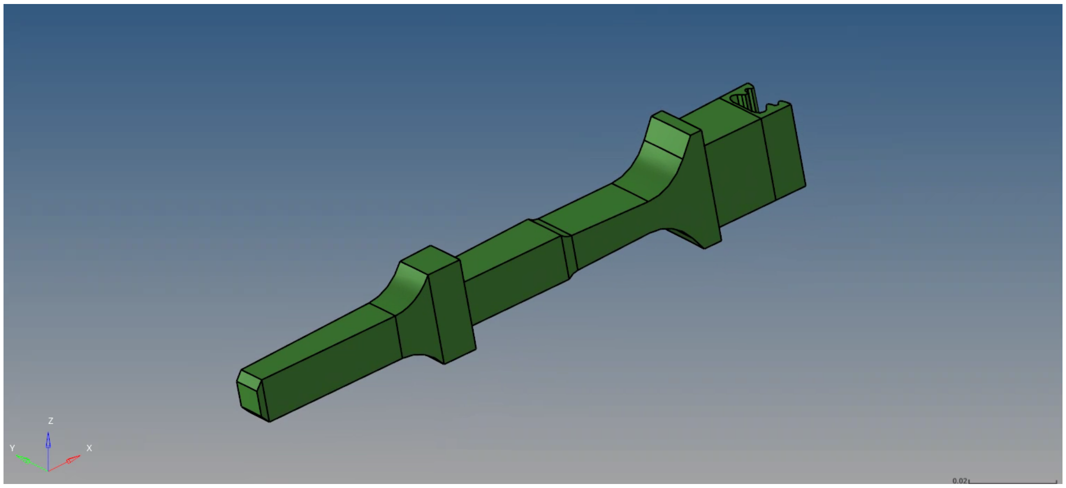

Figure 3.3: DISK.

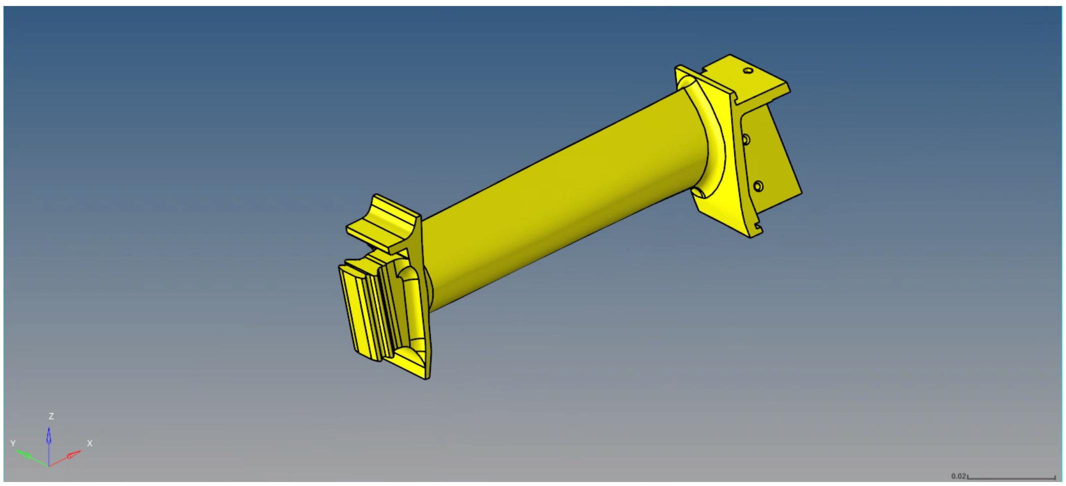

Figure 3.4: BLADE.

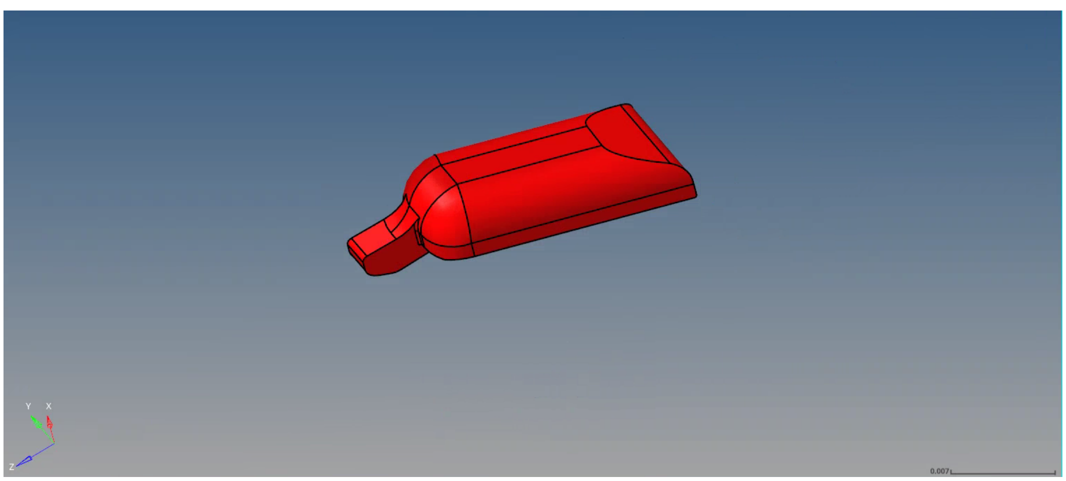

Figure 3.5: DAMPER (neglected).

In the next subsections how the mesh was done for each component will be briefly explained.

3.2.1 Disk

The disk has been divided in two part, the *lower* part and the *upper* part (fig 3.6).

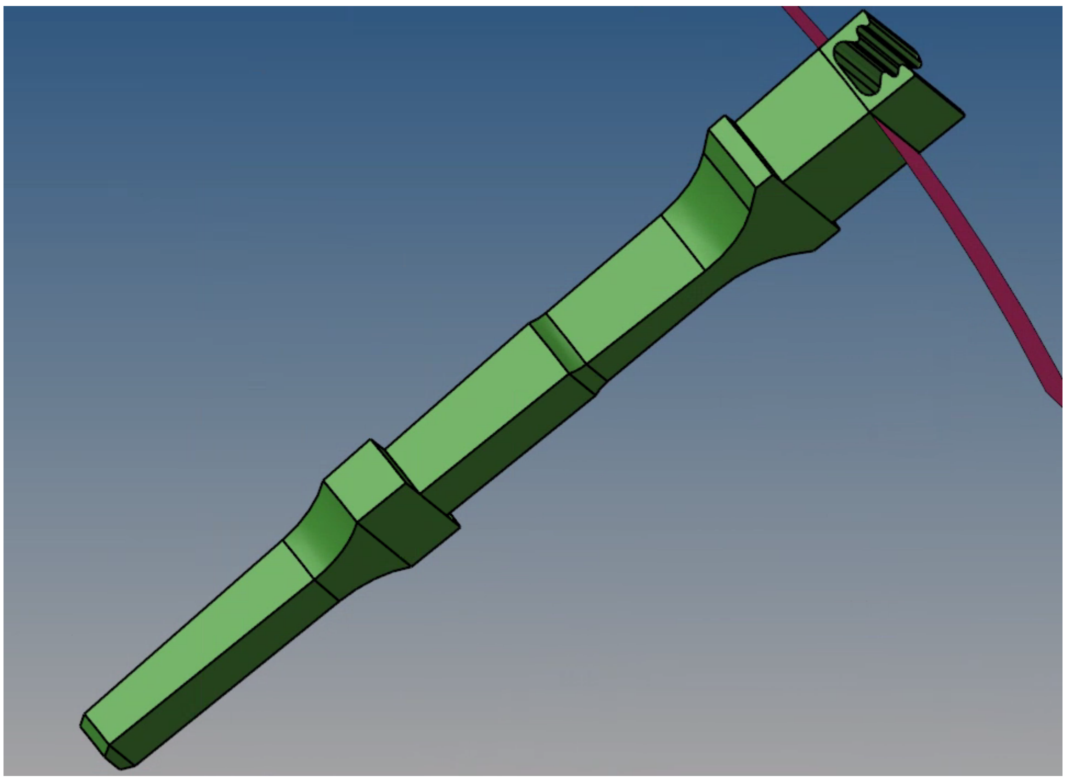

Figure 3.6: Disk divided in two parts.

As for the upper part, it is important to have a very good and detailed mesh, especially in the contact region with the blade. Indeed in this region it is important to generate a good mesh so that the elements of the disk coincide with those of the blade [4].

The steps followed for this part are:

[4]Further information about the contact region will be explained in the section 5.3.4

- *generation* of a detailed and refined 2D mesh using quad elements in one face of the upper part of the disk (fig. 3.7(a),(b));
- *drag* of the 2D mesh following the geometry along the side of the disk (fig. 3.7(b)). This step generates 3D hexa [5] elements.

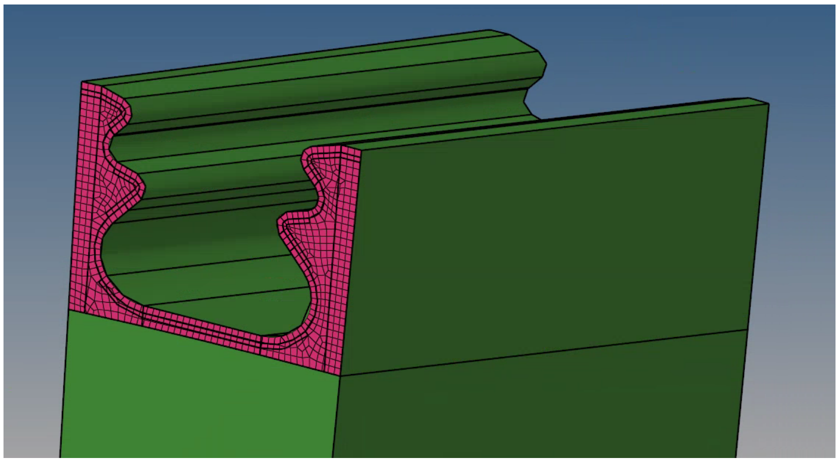

(a) 2D.

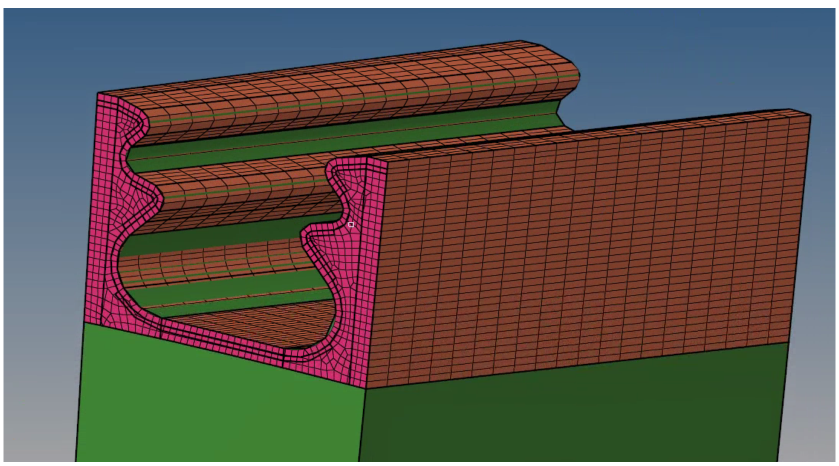

(b) 3D.

Figure 3.7: Mesh of the upper part of the disk.

As for the lower part, it was not important to have a detailed mesh. This is the procedure followed for this region:

[5]Hexa are solid elements that have the shape of a prism.

- *generation* of a coarse 2D mesh in the the side of disk (fig. 3.8(a));
- *spin* of the 2D quad elements of an angle equal to $IBPA = \dfrac{360}{N} = 2.4657°$ (fig. 3.8(b)). The result of this spinning operation is the generation of a 3D mesh composed by hexa elements.

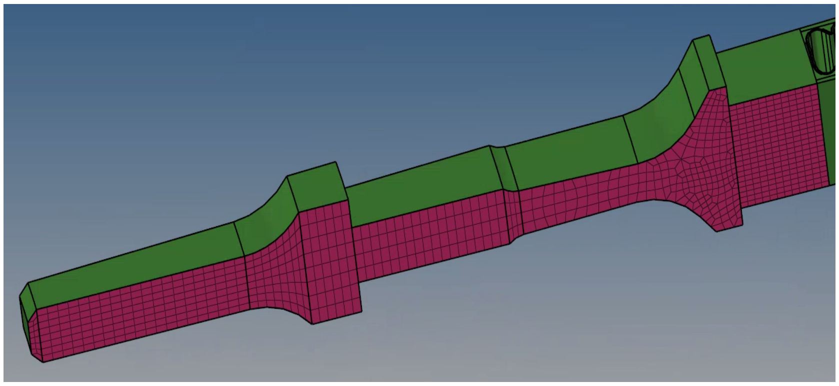

(a) 2D.

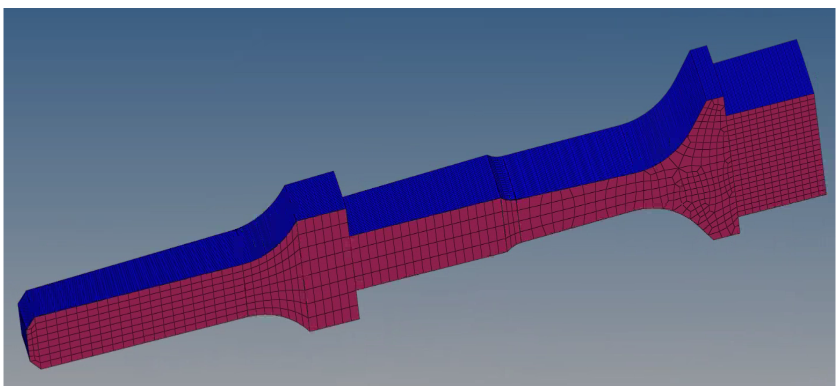

(b) 3D.

Figure 3.8: Mesh of the lower part of the disk.

3.2.2 Blade

As for the blade, it has been divided into four parts:

- the lower part of the *shank*;
- the upper part of the *shank*;

- the *airfoil*;
- the *shroud.*

3.2.2.1 Shank

The shank is the part of the blade that is in contact with the disk.

In this case it has been divided in two parts: lower and upper (fig 3.9).

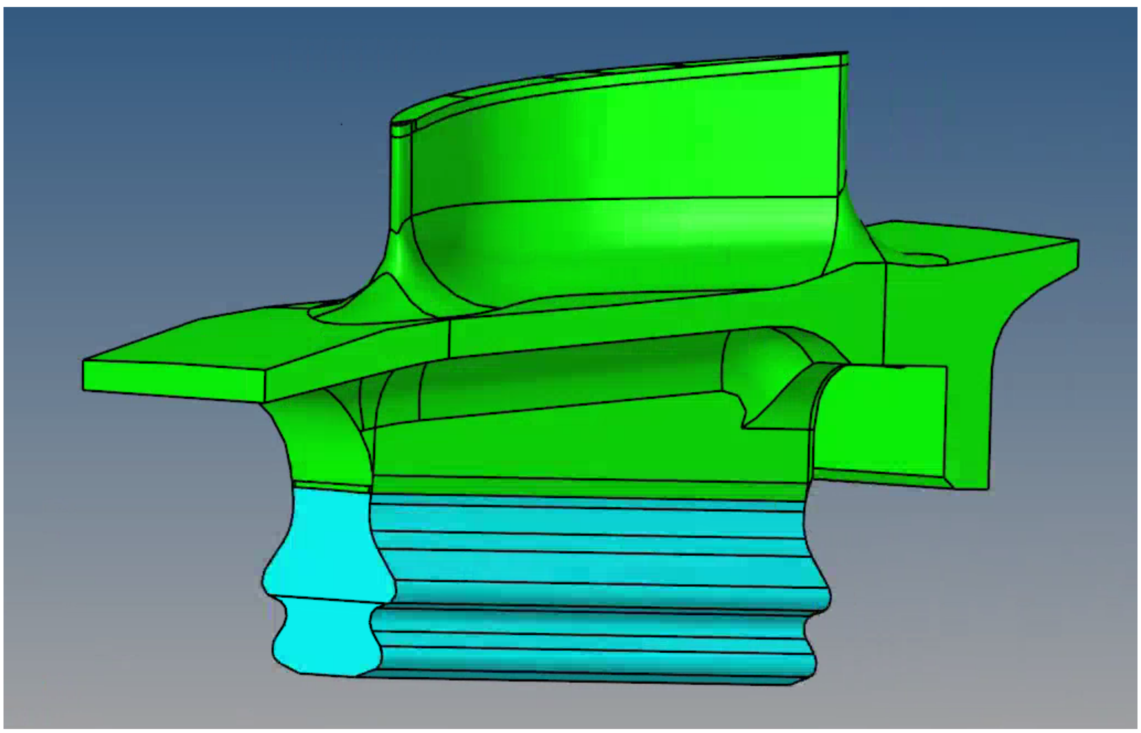

Figure 3.9: Shank divided in two parts.

The lower part (sometimes called "dovetail") is the one that is in contact with the disk. To mesh this part the procedure is the same of the upper part of the disk, i.e.:

- *generation* of a detailed and refined 2D mesh using quad elements, making sure that the elements of the contact between the disk and the blade have matched nodes (fig. 3.7(a),(b));

- *drag* of the 2D mesh following the geometry along the side of the shank. This step generates 3D hexa elements.

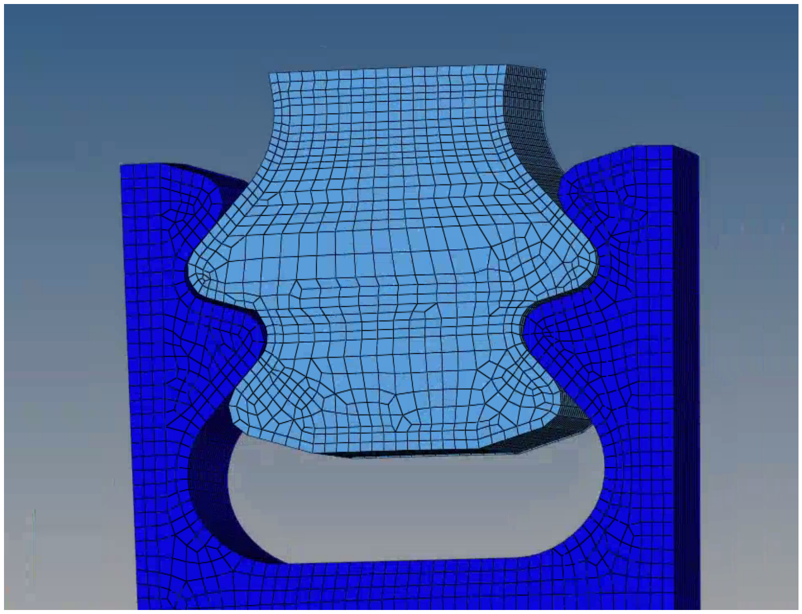

(a)

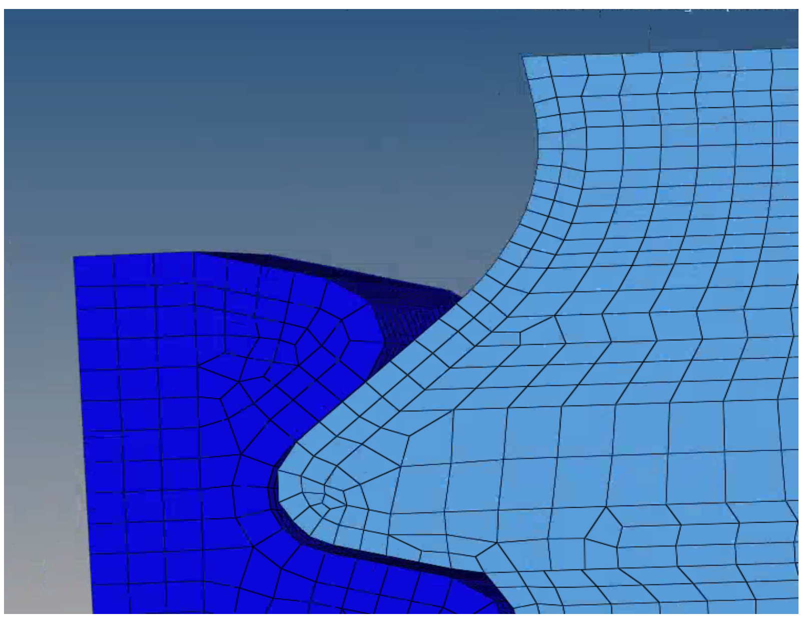

(b) Detail of one of the four contact regions.

Figure 3.10: Mesh of the lower part of the shank.

The upper part was meshed using tetra elements [6], because this kind of element is more fitted for portion where the geometry is complicated. For doing this procedure the steps are:

- *generate* a 2D mesh for the skin of the component with trias;
- '*fill*' the skin by using the command tetramesh.

The result is shown in fig 3.11.

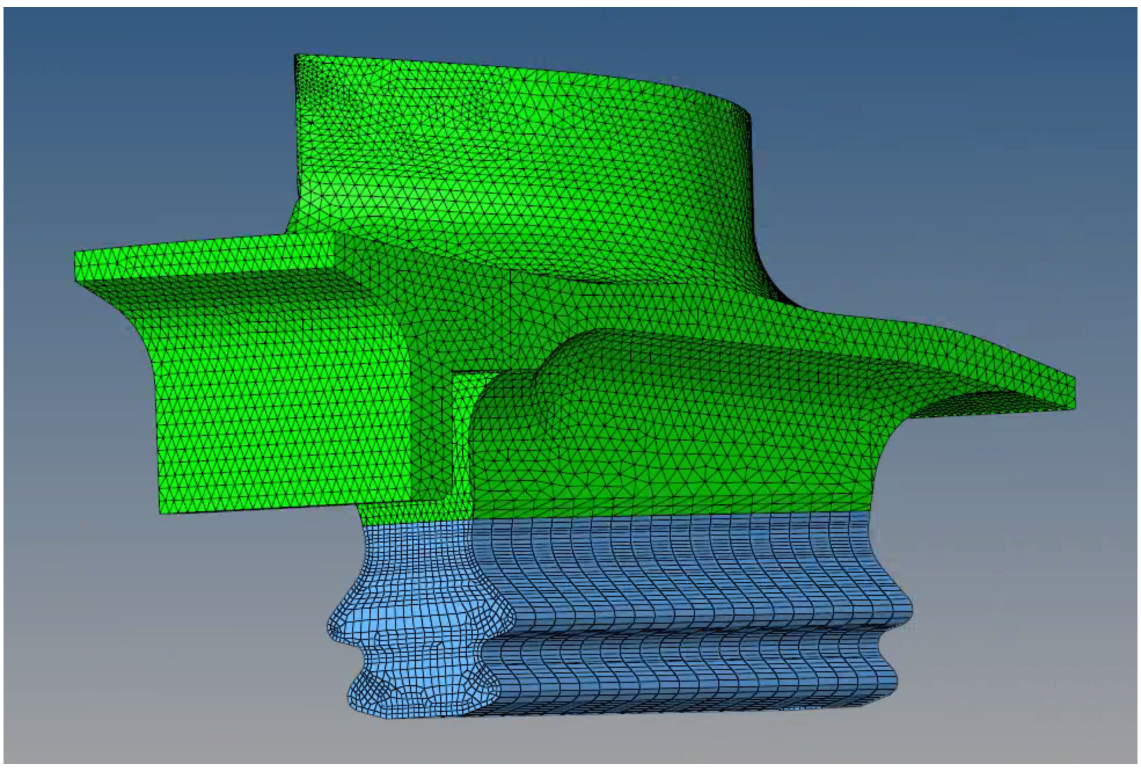

Figure 3.11: 3D mesh of the shank.

3.2.2.2 Airfoil

As for the airfoil, the technique used was the same seen before:

- *generation* of a detailed 2D mesh using quad elements in the airfoil section (fig. 3.12(a));

[6]Tetras are solid elements that have the shape of a pyramid.

- *drag* of the 2D mesh following the geometry along the airfoil spanwise (fig. 3.12(b)). This step generates 3D hexa elements.

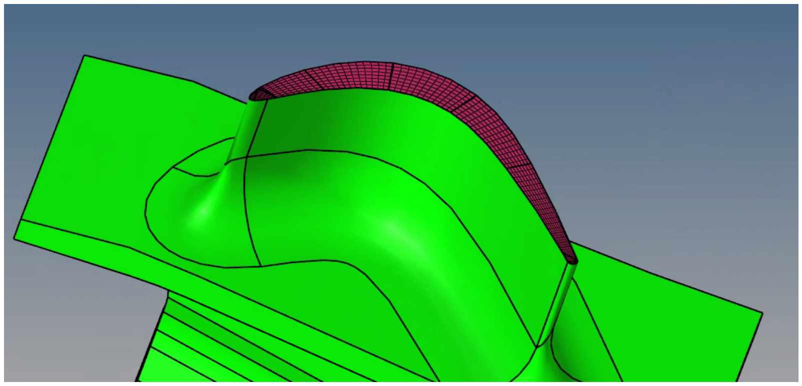

(a) 2D.

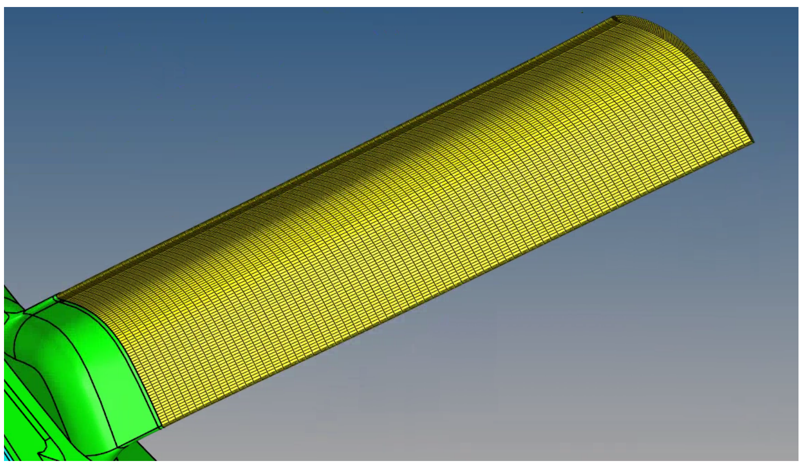

(b) 3D.

Figure 3.12: Mesh of the airfoil.

3.2.2.3 Shroud

The last portion of the blade is the shroud.

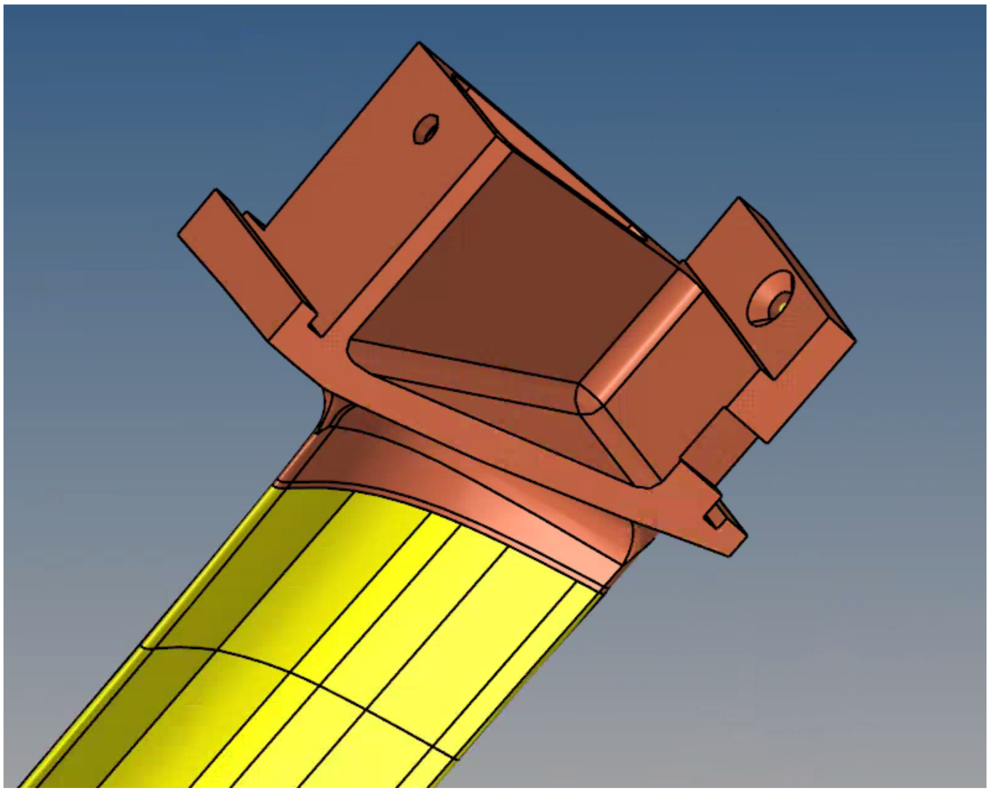

Figure 3.13: Shroud.

For this region the mesh was done using tetra elements because of the complexity of the geometry. So, as written for the shank:

- *generate* a 2D mesh for the skin of the shroud with trias;
- '*fill*' the skin by using the command tetramesh.

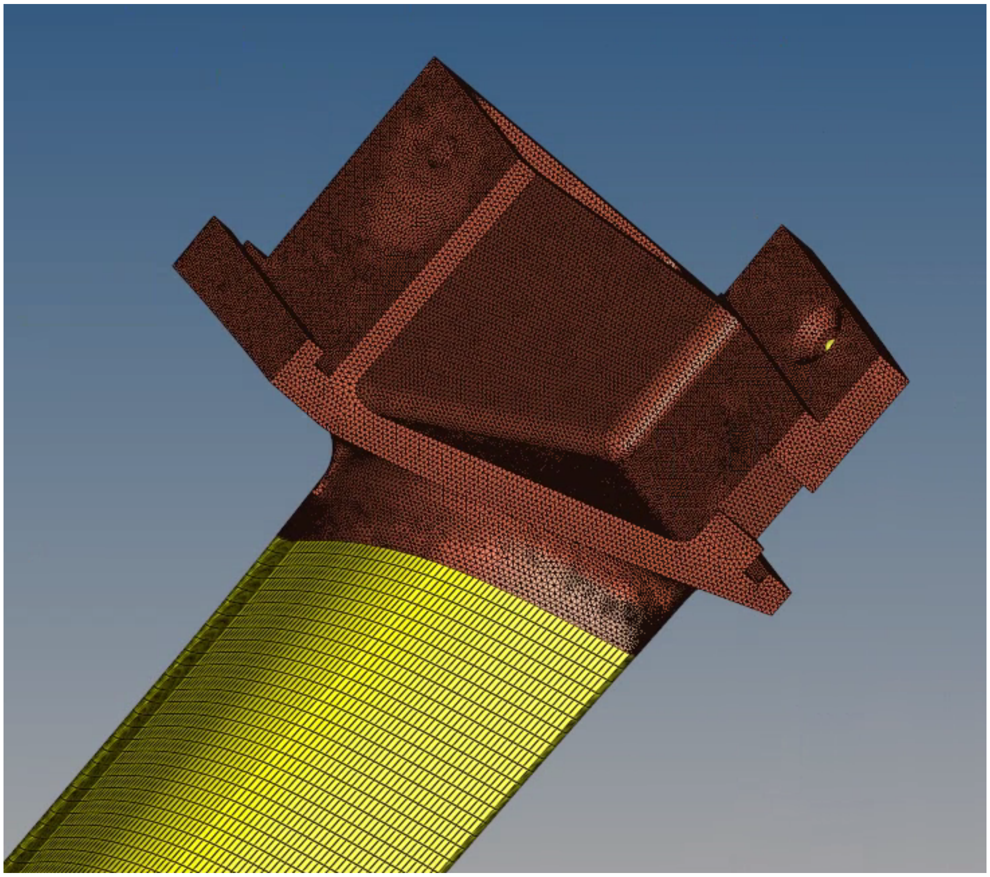

Figure 3.14: 3D mesh of the shroud.

3.2.3 Definition of contact regions

To complete the FEM model it is important to define the contact regions. For ARIAS bladed disk the contact between blade and disk takes place in four areas (fig. 3.15), two for each side of the disk (and obviously also of the shank). As written before, the 3D mesh of the dovetail and of the disk was created so that each contact area were precisely discretized with HEXA elements.

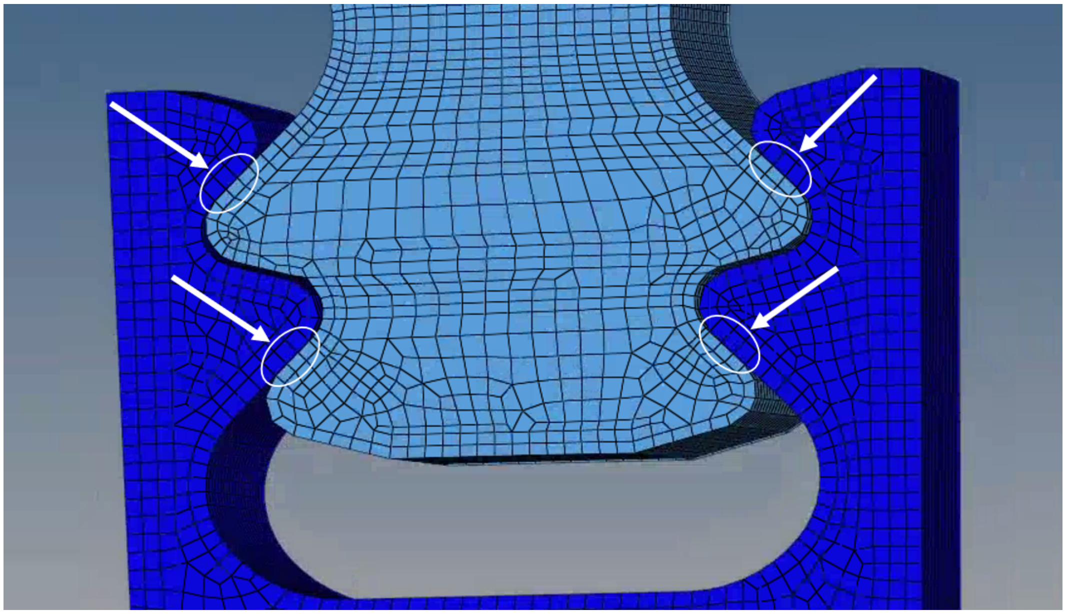

Figure 3.15: 3D mesh of the shroud.

In figure 3.16 the four contact regions defined using Hypermesh are shown.

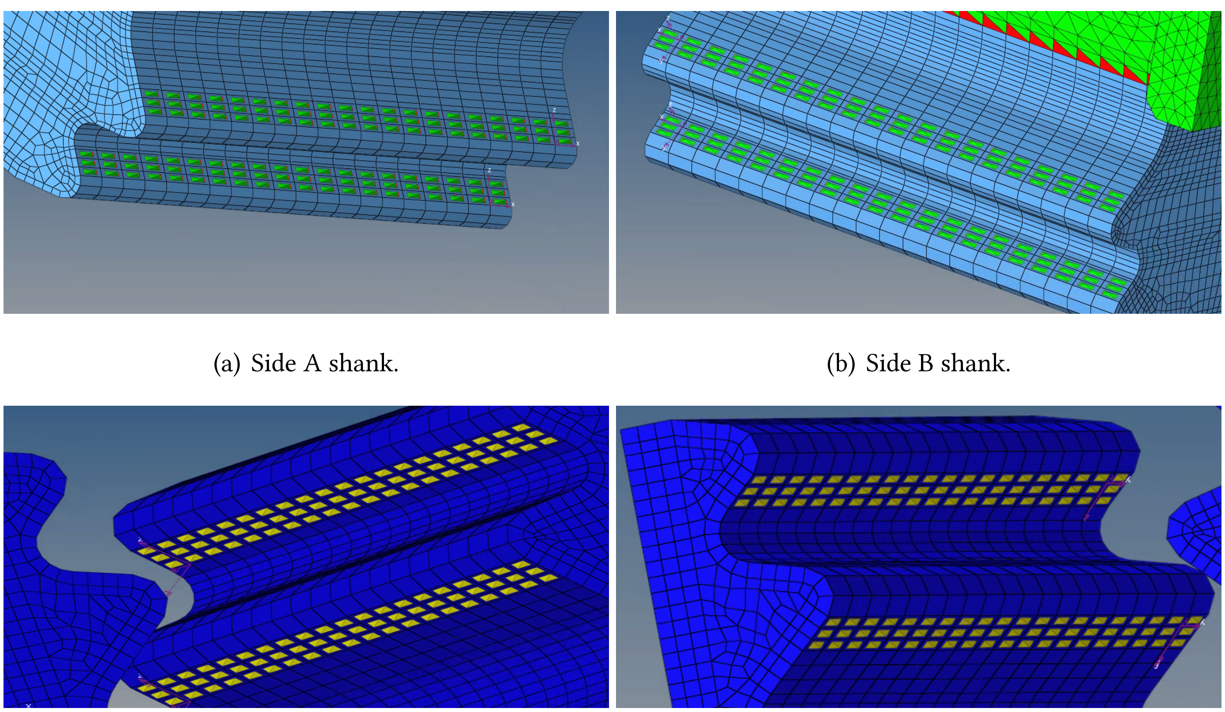

(a) Side A shank.

(b) Side B shank.

(c) Side A disk.

(d) Side B disk.

Figure 3.16: Contact regions.

3.2.4 Set of nodes for boundary conditions

The last step done using Hypermesh is to create a set of nodes in which the boundary condition will be applied with Ansys. These set of nodes is located in the disk flange, as it is possible to see in figure 3.17.

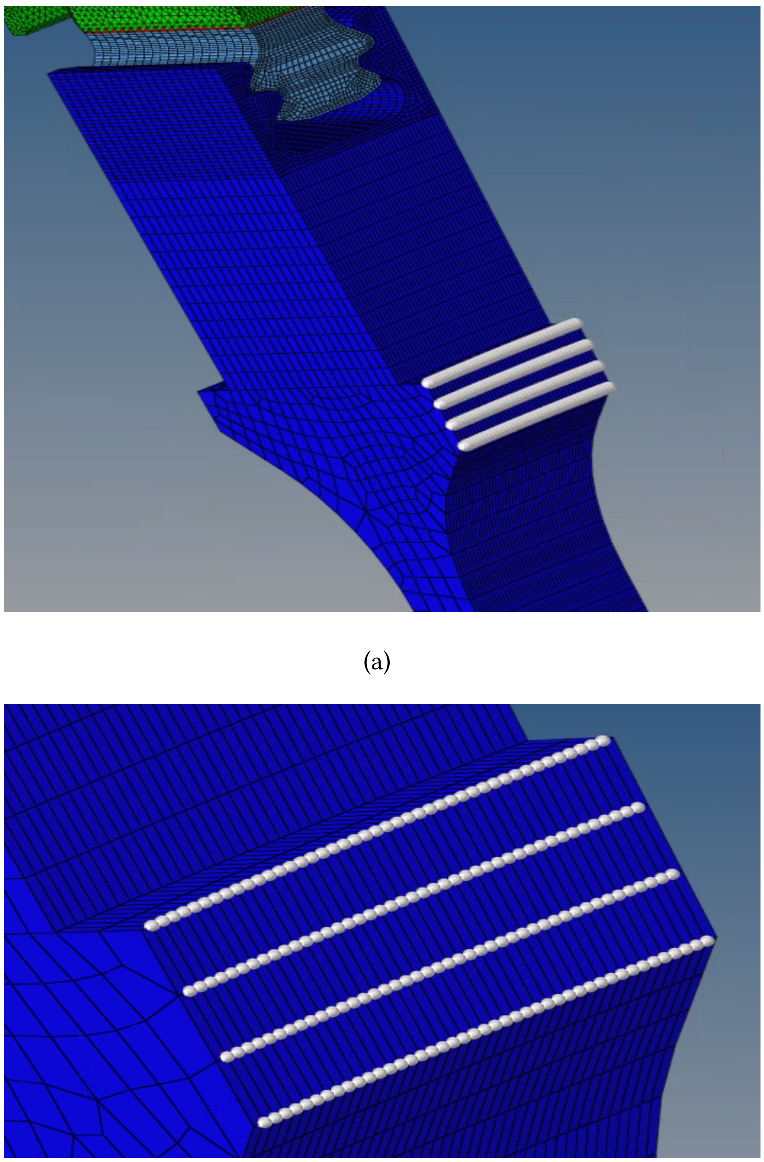

(a)

(b)

Figure 3.17: Set of nodes for setting the BC.

3.2.5 Final FEM model

As written in the previous paragraphs, just a very quick explanation of how the 3D mesh was obtained for the bladed disk was done. After all these steps, the final result of the 3D mesh is shown in the following figure 3.18.

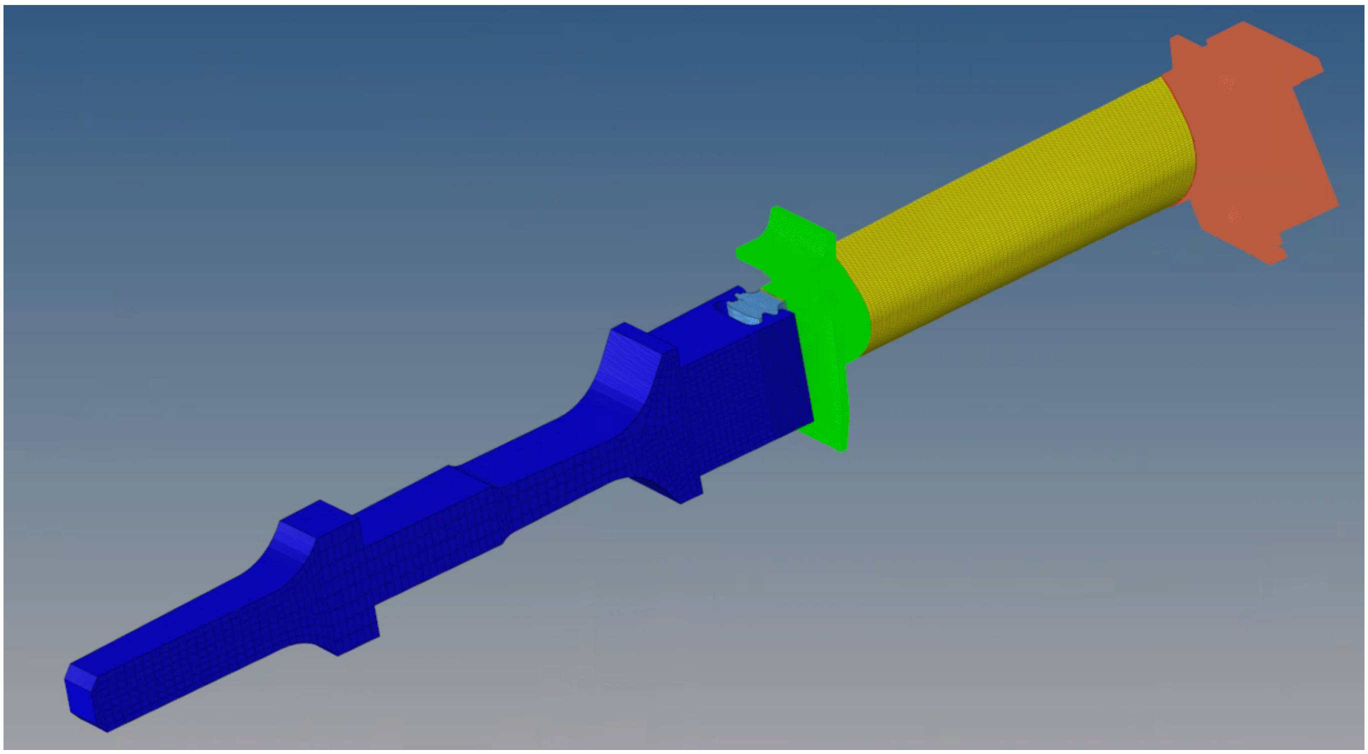

Figure 3.18: Complete 3D model.

3.3 Impact of the fem mesh order in a modal analysis

The first task done in this thesis is the study of the impact of the fem mesh order in a modal analysis.

In general, the second-order elements are more precised because they have a higher value of nodes, but they imply also a higher computational cost for the analyses. As written before tetra elements are more suited for regions where the geometry is complicated, but they are also less precised so they have been used always as second order elements. As for hexa, we want to understand the impact of using first-order versus second-order in the results of a modal analysis.

So, starting from the model of fig. 3.18, two different FEM model were generated:

- **model A**, with first-order hexa and second order tetra;
- **model B**, with both hexa and tetra of second order.

In the following table 3.1 the characteristics of the two models are summarized.

	Model A	Model B
Number of elements	782692	782692
Number of nodes	1115285	1499689
HEXA	FIRST ORDER	SECOND ORDER
TETRA	SECOND ORDER	SECOND ORDER

Table 3.1: Comparison between model A and B

In the following figure 3.19 it is possible to see the different amount of nodes for hexa elements between **model A** (fig. 3.19 (a), 3.20 (a)) and **model B** (fig. 3.19 (b), 3.20 (b)).

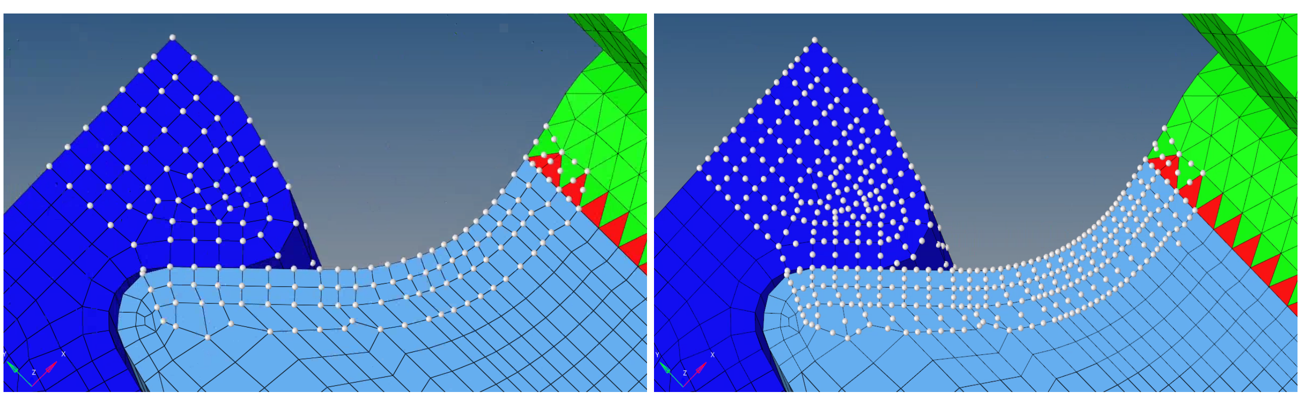

(a) Model A. (b) Model B.

Figure 3.19: Difference between the two models. (1)

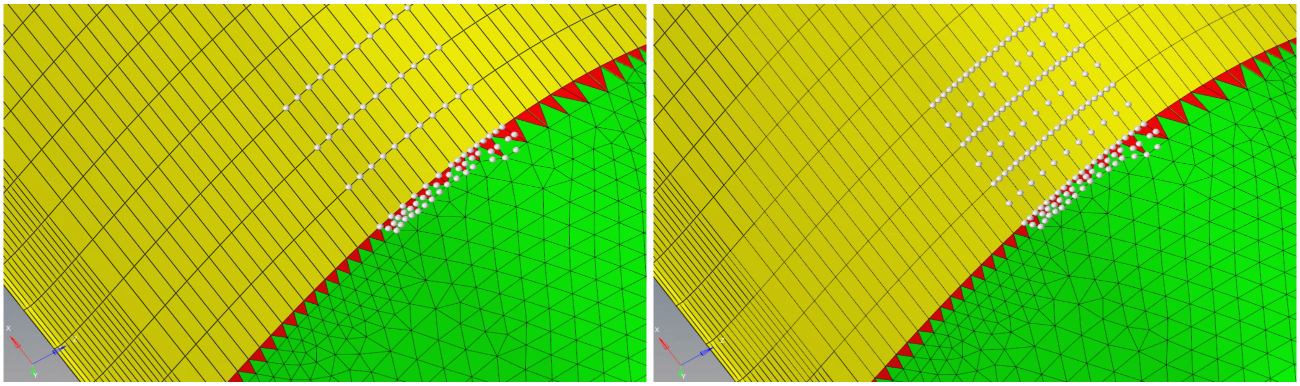

(a) Model A.

(b) Model B.

Figure 3.20: Difference between the two models. (2)

3.3.1 Modal analysis

For both model A and B a modal prestressed analysis has been performed using Ansys APDL.

3.3.1.1 Pre processing

Before running the analysis, the follwing conditions were imposed:

- operative speed imposed at $\Omega = 2850 rpm$;
- temperature effects are not considered, so it was imposed a uniform temperature equal to the reference temperature, $T_{UNIF} = T_{REF} = 25°C$;
- axial and tangential DOFs locked for a group of nodes in the disk flange (see fig 3.21);
- cyclic symmetry, with $N = 146$ and $IBPA = \frac{360}{N} = 2.4657°$;

- blade/disk interfaces are modeled with MPC [7] (see fig 3.22);
- associate the material properties to the 3D mesh.

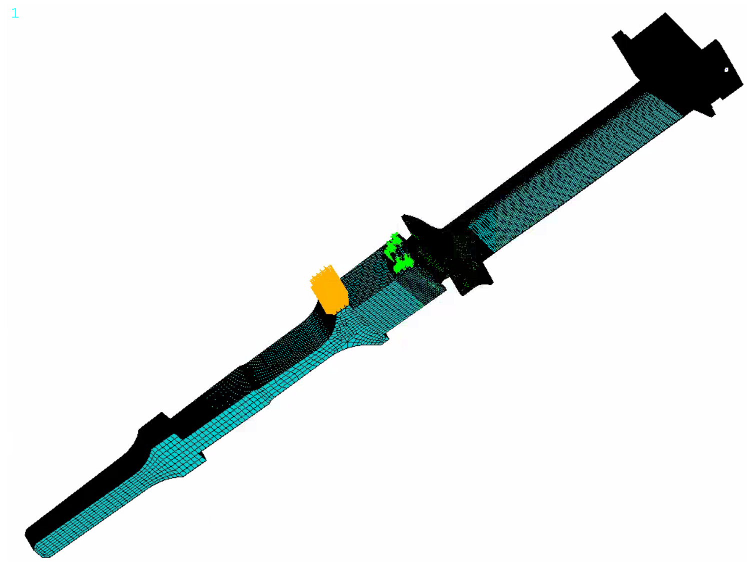

Figure 3.21: Axial and tangential DOFs locked for nodes highlighted in orange.

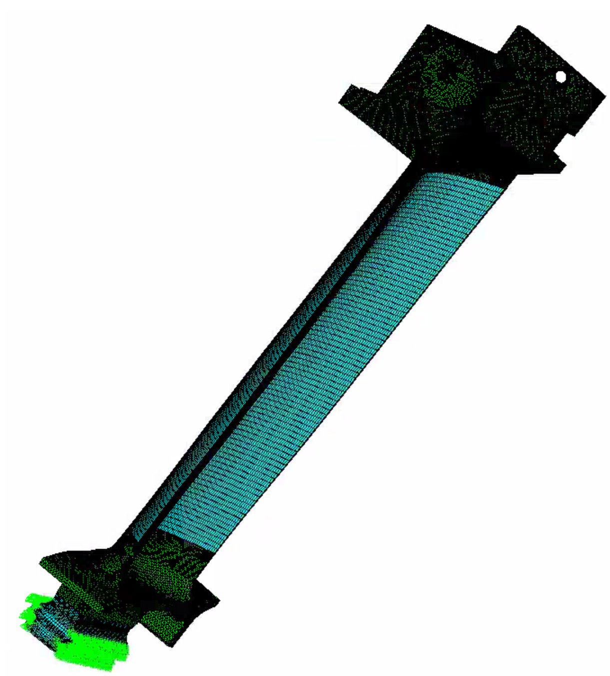

Figure 3.22: Blade/disk contact modeled with MPC elements.

[7] MPC means multipoint constraint approach. It is a contact model of Ansys APDL for bonded and no-separation contact definitions, which can be used with solid-solid assembly, i.e. both contact and target surfaces paste onto solid element faces [16, 17].

3.3.1.2 Run settings

As for the analysis, it was composed by two steps:

- *step 1*: a non linear static analysis to evaluate the prestress effects;
- *step 2*: the modal analysis taking into account softening/stiffening effects calculated in *step 1*.

As for modal cyclic symmetry options, it was calculated the first three modes for all the harmonic indices, so from $HI = 0$ to $HI = \frac{N}{2} = 73$.

3.3.2 Results

For **model A** the analysis lasted 11 hours while for **model B** it lasted 21 hours. This is in line with what we expected since the second model has many more nodes than the first.

As written in the previous chapter, the outputs of a modal analysis are the values of natural frequencies and the relatives modal shapes.

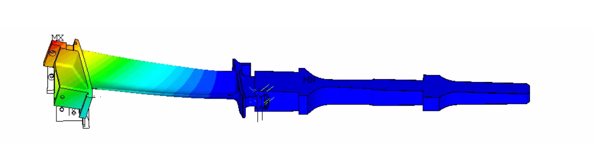

(a) 1^{st} mode, $f = 184Hz$.

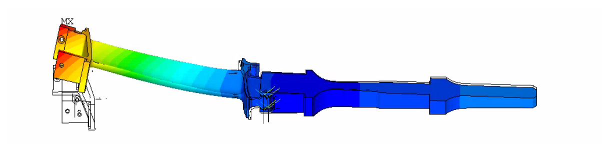

(b) 2^{nd} mode, $f = 442Hz$.

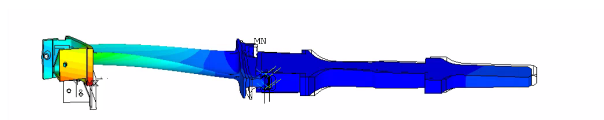

(c) 3^{rd} mode, $f = 4212Hz$.

Figure 3.23: First three modes of model A, with $HI = 1$.

3.3.2.1 Natural frequencies

The comparison between natural frequencies calculated for the two models is shown in the following table 3.2.

MODE	Harmonic Index	$f_A[Hz]$	$f_B[Hz]$	$\frac{\lvert f_A - f_B \rvert}{f_A}[\%]$
1^{st} mode	1	205.10	204.16	0.4583
1^{st} mode	36	206.53	205.94	0.2857
1^{st} mode	71	206.29	205.71	0.2812
2^{nd} mode	1	451.57	440.45	2.4625
2^{nd} mode	36	529.73	529.01	0.1359
2^{nd} mode	71	532.87	532.15	0.1351
3^{rd} mode	1	4239.9	4225.6	0.3373
3^{rd} mode	36	5552.0	5548.4	0.0648
3^{rd} mode	71	5572.1	5568.4	0.0664

Table 3.2: Comparison of natural frequencies.

As it is possible to see in the table, there are no significant differences between the frequencies calculated for the model A and the ones of model B.

3.3.2.2 Modal shapes

In addition to the frequencies, also the mode shapes must be compared. We need to compare corresponding modes obtained from model A and model B and verify that they are consistent. In order to do this, it has been used a company tool called *Modal Assurance Criterion (MAC)*.

MAC As written before, the Modal Assurance Criterion is a tool used to compare modal vectors. The MAC is calculated as the normalized scalar product of the two sets of vectors $\{\phi_A\}_r$ and $\{\phi_B\}_q$. The resulting scalars are arranged into the MAC matrix

[20]:

$$MAC = \frac{|\{\phi_A\}_r^T \{\phi_B\}_q|^2}{(\{\phi_A\}_r^T \{\phi_A\}_r)(\{\phi_B\}_q^T \{\phi_B\}_q^T)} \tag{3.1}$$

An equivalent and clearer formulation for the MAC is:

$$MAC = \frac{|\sum_{j=1}^{N} \{\phi_A\}_j \{\phi_B\}_j|}{(\sum_{j=1}^{N} \{\phi_A\}_j^2)(\sum_{j=1}^{N} \{\phi_B\}_j^2)} \tag{3.2}$$

MAC can assume values between 0 and 1:

- $MAC = 0$ for not consistent modes;
- $MAC = 1$ for fully consistent modes.

Values larger than 0.9 indicate consistent correspondence whereas small values indicate poor resemblance of the two shapes [20].

Modal shapes results The results of the comparison of corresponding modes of the two models are shown in the table 3.3. Not all the harmonic indices have been reported, but only some.

In conclusion, model A produces same model B results but in shorter time (50%). So it is better for modal analysis to have first order hexa elements in the FEM model.

MODE	Harmonic Index	MAC
1st mode	1	1.0000
1st mode	36	1.0000
1st mode	71	1.0000
2nd mode	1	0.9998
2nd mode	36	1.0000
2nd mode	71	1.0000
3rd mode	1	0.9998
3rd mode	36	1.0000
3rd mode	71	1.0000

Table 3.3: Comparison of modes.

3.4 Post processing

As you can see in figure 3.1, after performing a modal analysis there are many post-processing activities that need to be done to process the results. Some examples are:

- modal shape recognition;
- generation of report file to compare analytical results with experimental results;
- generation of report file for flutter analysis;
- generation of FreND diagram;
- generation of Campbell diagram;
- generation of Goodman diagram;
- etc.

In this thesis some of these activities have been considered, with the aim of optimizing the procedure and speeding up the execution times. These activites are: modal shape

recognition; generation of FreND diagram; generation of report file for flutter analysis.
The results used for this part derive from modal analyses performed for model A (see section 3.3). This analyses have all the same characteristics of the one of chapter 3.3.1., the only difference is the number of harmonic indices that have been taken into account.
All the postpro activities have been done using Ansys APDL and Matlab.

3.4.1 Modal shape recognition

The first aspect considered is the modal shape recognition.
This aspect is very important to understand what is the vibration mode of the blade at a given natural frequency calculated in the modal analysis.
For this aspect it has been extracted the first ten modes for each of the following harmonic indices: $HI = 1, 8, 15, 22, 29, 36, 43, 50, 57, 64, 71$. So in total there are 110 modes (or 55 complex modes).
The current process for modal shape recognition consists in the following steps:

- open APDL (3.24(a))
- go on post processing section (3.24(b))
- load the file with the results (3.24(c))

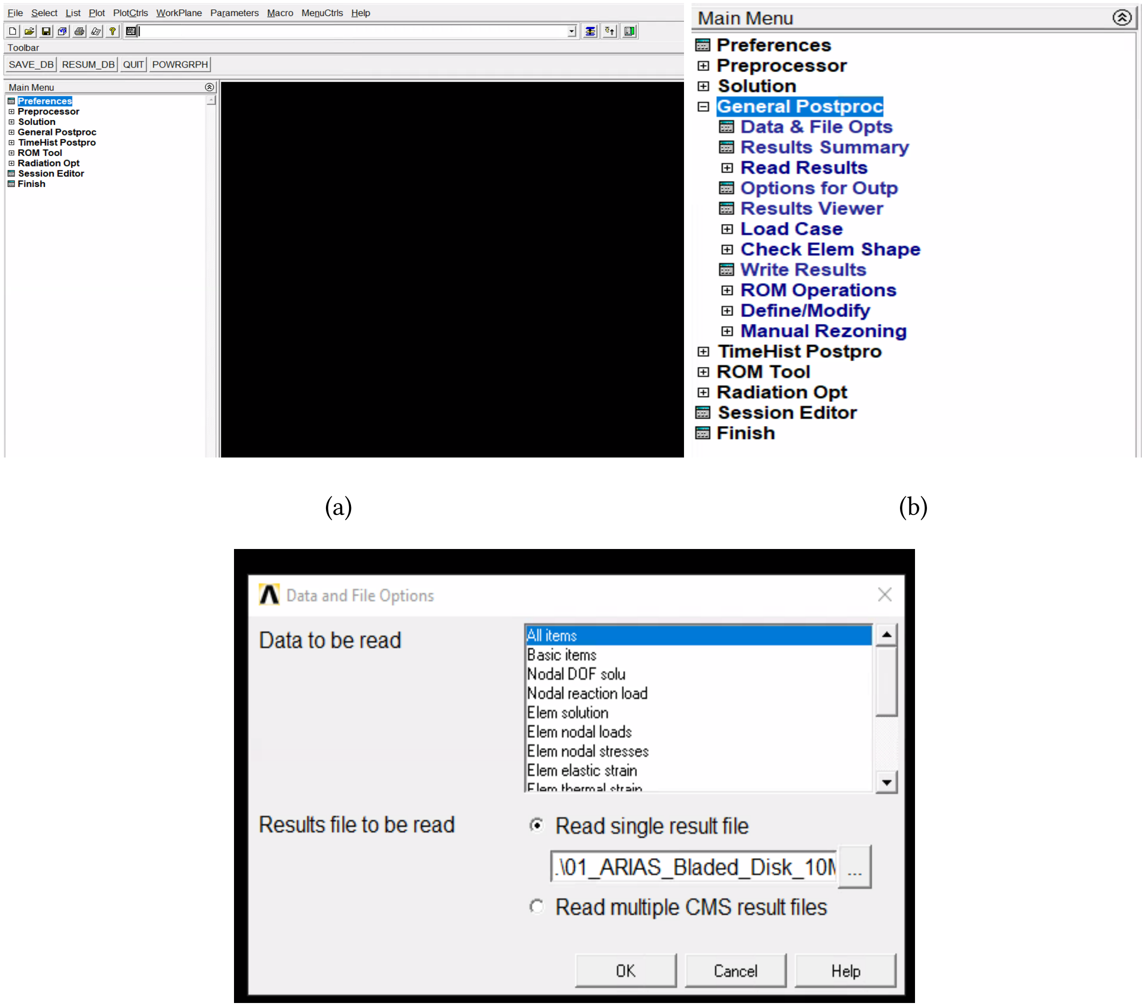

(a) (b)

(c)

Figure 3.24: First steps for modal shape recognition.

Then, for each mode:

- load the relative load step (3.25(a));
- select the solution to plot, that in this case are displacements (3.25(b));
- plot the result, move the model and save some pictures (3.25(c),(d),(e)).

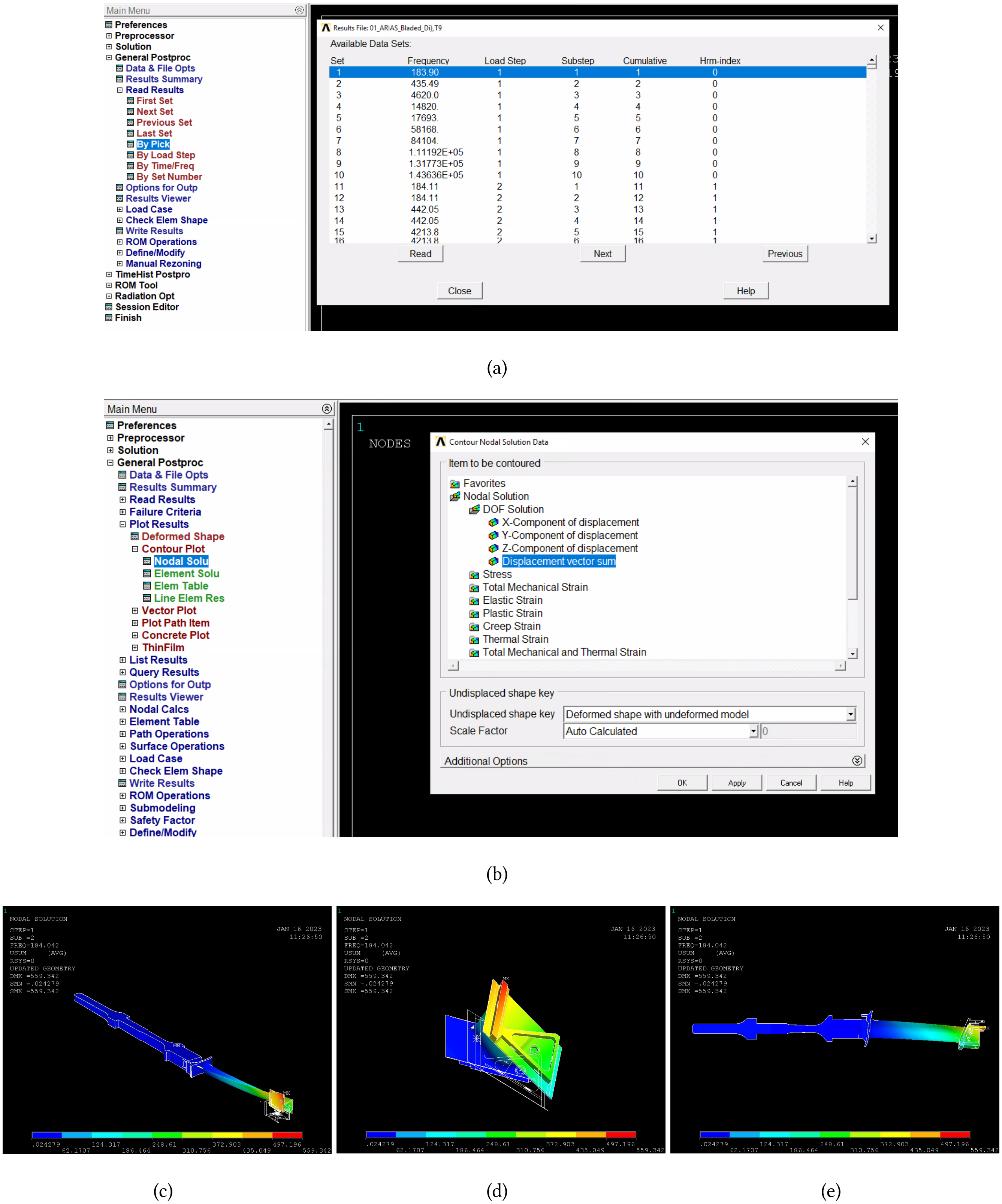

Figure 3.25: Other steps for modal shape recognition.

These pictures then will be used to recognize the modal shape.

Considering all the 55 modes, this procedure lasts almost 200 minutes. To speed up the process an APDL macro has been designed. Thanks to this macro all these steps are carried out autonomously by APDL. The user therefore only needs to run the macro after setting some parameters in the macro itself and wait to get the output images.

For the example taken into account, to get the three images for all the extracted modes, the macro took 45 minutes, reducing time by 77%.

Some examples of these pictures are shown in the following figures 3.26,3.27 and 3.28.

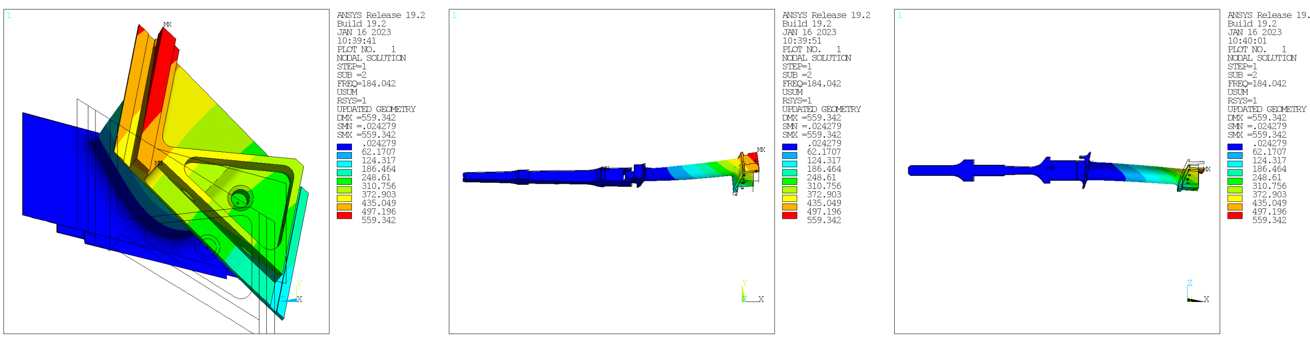

(a) Top view. (b) Side view. (c) Right view.

Figure 3.26: $HI = 1, f = 184Hz$.

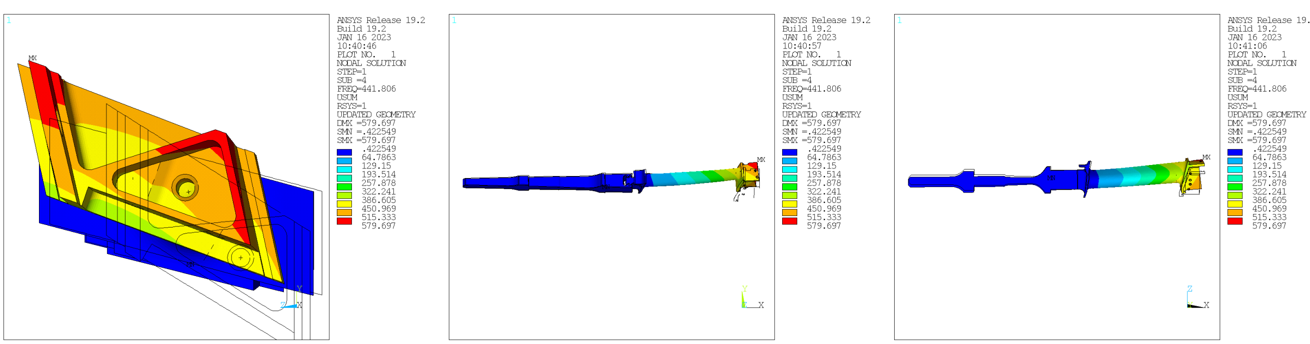

(a) Top view. (b) Side view. (c) Right view.

Figure 3.27: $HI = 1, f = 442Hz$.

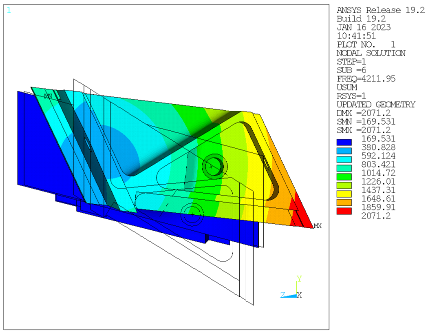

(a) Top view.

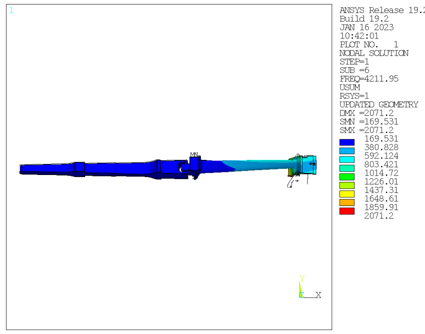

(b) Side view.

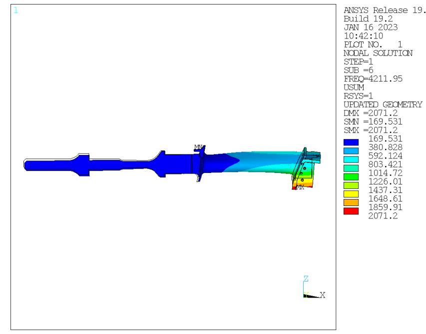

(c) Right view.

Figure 3.28: $HI = 1$, $f = 4212Hz$.

Furthermore, the macro was designed to work in the enterprise compute cluster as well. This has brought several advantages: in addition to saving time, thanks to the cluster the user can carry out various activities in parallel, thus avoiding having APDL busy and so not being able to work. Furthermore, thanks to the greater computational power of the cluster, images of the entire disk can be obtained by expanding the solution to more sectors (fig 3.29, 3.30, 3.31).

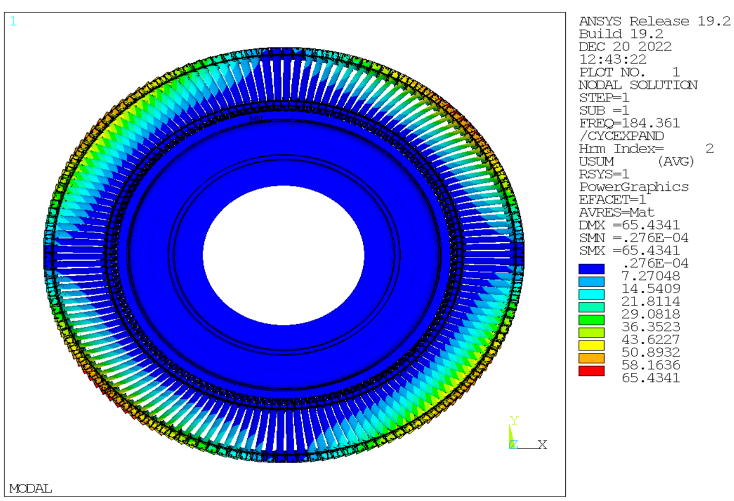

(a) Front view.

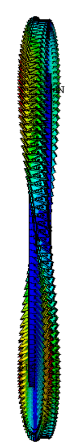

(b) Side view.

Figure 3.29: $HI = 2$, $f = 184.36Hz$.

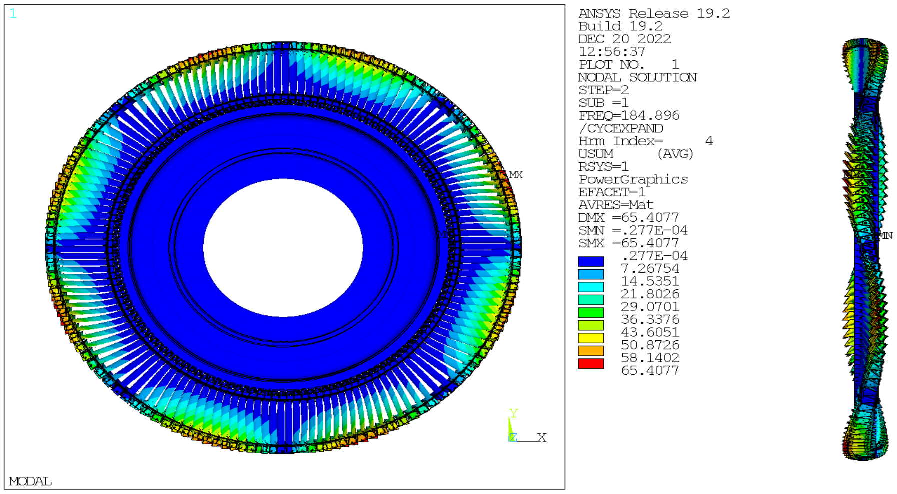

(a) Front view.

(b) Side view.

Figure 3.30: $HI = 4$, $f = 184.89Hz$.

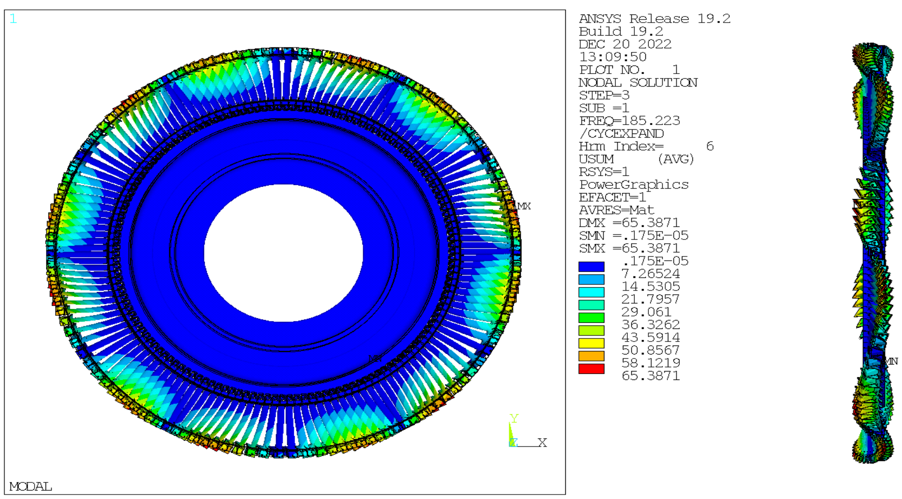

(a) Front view.

(b) Side view.

Figure 3.31: $HI = 6$, $f = 185.22Hz$.

All the advantages are summarized in the following table 3.4.

	Current	Optimize - Step 1	Optimize - Step 2 (cluster)
Time reduction	-	77%	70%
Other activities in parallel	no	no	yes
Enable 360° plot	no	no	yes

Table 3.4: Advantages obtained thanks to the macro.

3.4.2 FreND generation

The second postpro activity that has been optimized is the generation of FreND diagram. As expalined before, this plot has in the x-axis the nodal diameter and in the y-axis the frequency and describes how the value of the natural frequency of a mode shape changes with respect with the nodal diameter.
The current process to obtain this diagram starting from the results of a modal analysis is hand writing the values of nodal diameters and the relative natural frequencies one at a time and then plot them.
To optimize the process, a simple tool has been implemented. This tool is composed by:

- an APDL macro to extract the values of nodal diameters (i.e. harmonic index) and the relative natural frequencies and to write them in a text file;
- a matlab script to plot the data.

The result is a simpler and less tedious procedure. The diagram shown in figure 3.32 is about a modal analysis performed for ARIAS bladed disk, for which the first eight modes (four complex modes) have been considered for each harmonic index up to $\frac{N}{2} = 73$.

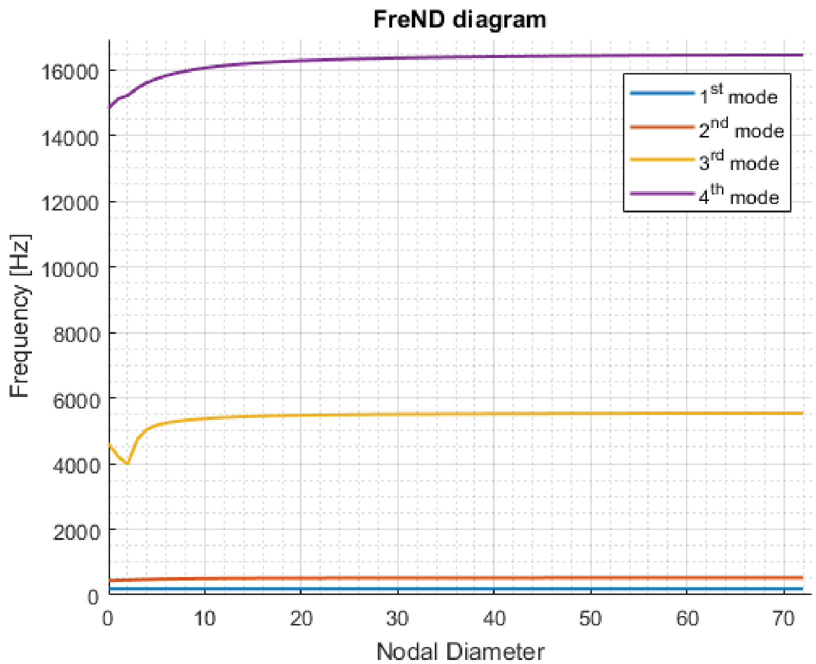

Figure 3.32: FreND diagram for the first four complex modes of ARIAS.

3.4.3 Generation of report file for flutter analysis

The last postpro aspect considered in this chapter is the generation of report file for flutter analysis. As explained before, this phenomenon must be studied to prevent the failure of the LPT.

To study flutter, in Avio Aero a specific tool is used. This tool requires input files containing results of modal analysis in **Nastran format**. In particular $N+2$ files is needed:

- a file that contains node locations;
- a file for elements/nodes connectivity;
- N report files corresponding to the N complex modes to be considered in the analysis, containing the nodal displacements.

Since Ansys is used as analysis software, there is a procedure to obtain these files and to transform the results from the Ansys format to the Nastran format.

This procedure turns out to be rather long and complex since it is composed of several APDL macros and the user has to go through many steps before obtaining all the necessary files described above (fig 3.33). Ideed there are:

- a first macro to obtain node locations;
- another macro to get the elements$\backslash$nodes connectivity;
- three macros that have to be launched for each complex modes to get nodal displacements. So if we need ten complex modes, we need to launch these three macros for ten times, so totally thirty times;
- finally it is necessary to rename all the $N + 2$ files in the correct way so that the flutter tool can read them.

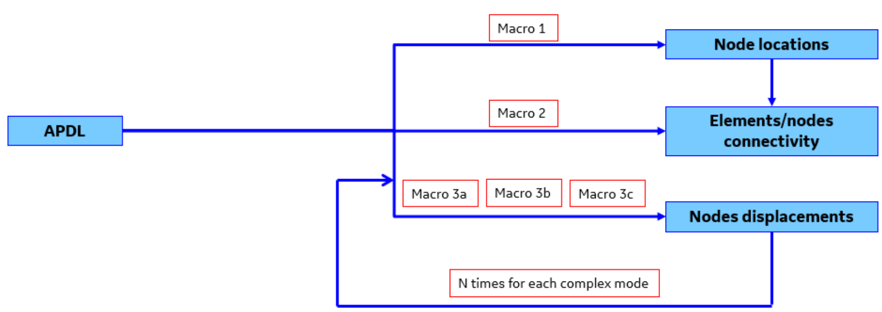

Figure 3.33: Procedure to obtain files for flutter analysis.

It has been considered an example in which twenty two complex modes were taken into account. For this example this procedure lasts almost 140 minutes without making any error. Indeed the bigger is the amount of steps, the easier is to make mistakes and in that case the procedure must be repeated, thus wasting even more time.

To speed up and simplify this procedure, a tool called 'Flutter converter' has been designed. It consists in six APDL macros (fig 3.35(a)) capable of generating all the necessary files autonomously (fig 3.34).

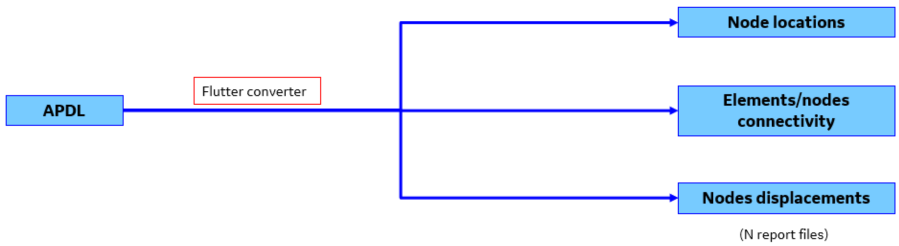

Figure 3.34: Simplified and optimized procedure.

To use this tool it is necessary to modify only a few parameters inside the 'Main_flutter' macro and then launch this in APDL. At the end there will be a folder (fig 3.35(b)) in which we will find all $N+2$ files correctly renamed (fig 3.35(c)).

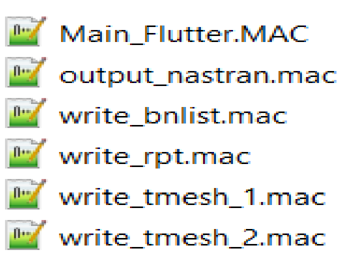

(a) 'Flutter converter' tool.

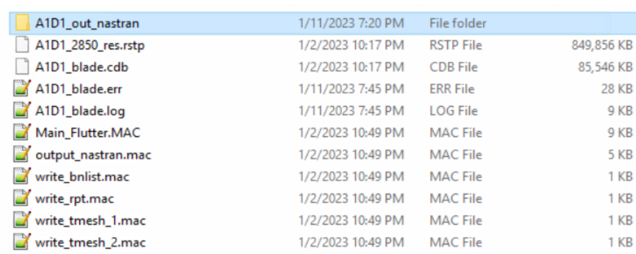

(b) Output folder.

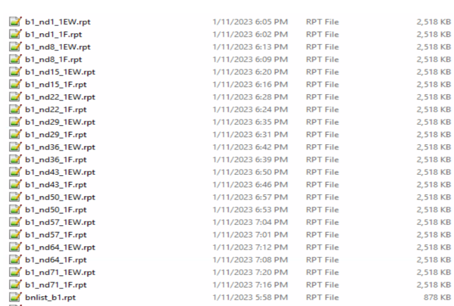

(c) Output files.

Figure 3.35: 'Flutter converter' tool with outputs.

So, thanks to this tool the process is very simplified, since only one step is required to obtain the files. In addition to this, the simplified procedure is also faster, in fact:

- if it is launched locally the time necessary to obtain all the files is 80 minutes, which implies a reduction of 43% of the times;
- if it is launched in the cluster the time necessary to obtain all the files is 7 minutes, which implies a reduction of 95% of the times (as well as the advantage of being able to do other activities in parallel).

All the advantages are summarized in the following table 3.5.

	Current	Optimize - Step 1	Optimize - Step 2 (cluster)
Time reduction	-	43%	95%
Other activities in parallel	no	no	yes

Table 3.5: Advantages obtained thanks to the 'Flutter converter' tool.

Chapter 4

Test data collection

In the last chapter of this thesis the theme of test data collection will be addressed. In particular this chapter is about the last part of the workflow for the study of a bladed disk, as it is possible to see in figure 3.1, which is reproduced below.

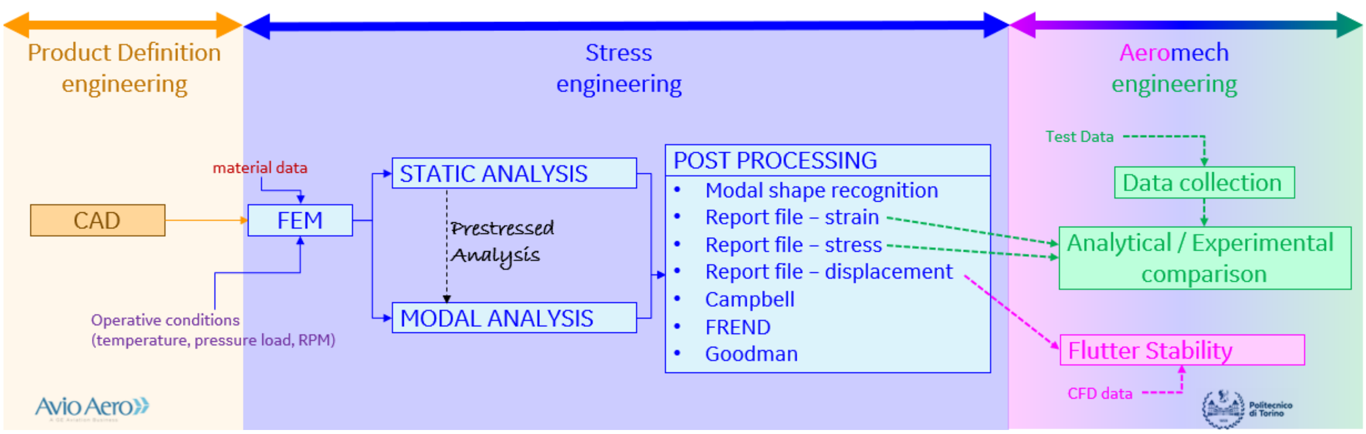

Figure 4.1: Workflow for the study of a bladed disk.

The test data collection is a very important phase because the experimental data will be compared with the analytical data. Besides, test data is necessary for writing the certification report, which is a very important document about the dynamic behavior of the turbine and which states that the component complies with all the requirements of the reference standard and therefore can be used in a aircraft engine.

All the test data that comes from an experimental test is raw data that needs to be post processed. In Avio Aero, after the post processing activity, data is loaded in a corporate TIBCO Spotfire Dashboard. This Dashboard is used as:

- collection of legacy data of several turbines of GE engines;
- database of responding modes of the relative LPT.

More detail about the Dashboard will be explained in the next sections.
The work done in this thesis was to load legacy data related to a GE program into the Dashboard starting from raw data that came from experimental tests already carried out.

4.1 Workflow

To add certification data of a legacy engine in the TIBCO Spotfire Dashboard the process consists in three main phases:

- *experimental tests*;
- *post pro* of experimental raw data;
- *upload and visualization* of post processed data in the Dashboard.

The workflow is illustrated in more detail in the figure 4.2.

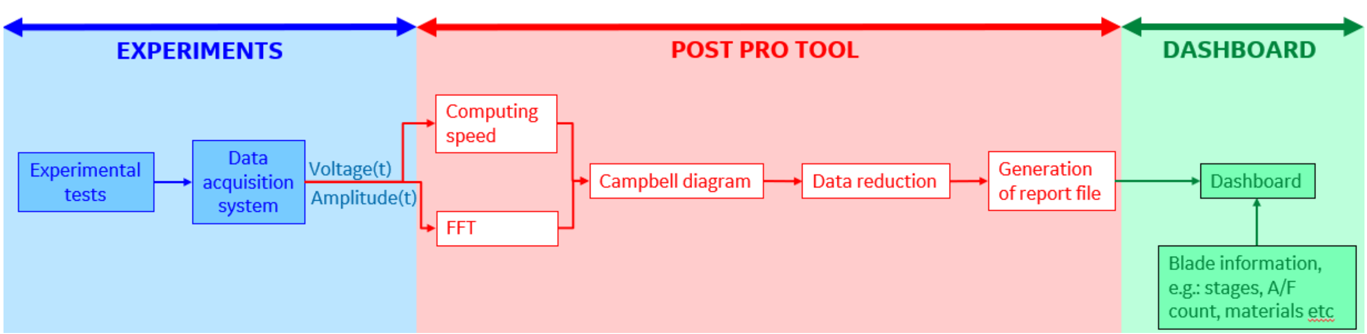

Figure 4.2: Workflow for test data collection.

Obviously, the process starts with the experimental test carried out for the specific component. Different sensors are used during the test, such as strain gauges, which measure strain by a change in resistance [1].

The measured data is firstly elaborated by a "DAQ", data acquisition system, which gives in output the raw data. These raw data consists in:

- data acquired from a speed sensor which contains information regarding the evolution of the electrical voltage measured by the sensor itself (in volts) as a function of time;
- data acquired from the strain gauges regarding the amplitude of the forced response as a function of time; the amplitude can be measured in terms of deformation, displacements or accelerations according to the modality and the sensors with which the test was carried out.

The work done in this thesis starts at this point, i.e. with the raw data already measured and ready to be post processed.

4.1.1 Postpro tool

To post process raw data it has been used a corporate Matlab tool called *postpro tool*. The main function of this tool are:

- compute the rotation velocity as a function of time starting from the voltage data of the speed sensor;
- calculate the Fast Fourier Trasfrom (*FFT*) of the amplitude of the forced response to switch between the time and frequency domains;

[1] That is only an example, there are several kind of sensor that are used during an experimental test; strain gauges are mentioned because they will be recalled in the section about the Dashboard.

- thanks to the previous two steps, the tool plot the Campbell diagram in which it is possible to see the responding modes of the LPT on which the tests were carried out;
- after this, the tool significantly reduces the amplitude data, filtering only the values higher than a certain set threshold;
- finally, the reduced data are written into a report file that will be used as input for the Dashboard.

Therefore, starting from the raw data of the reference GE program, the tool was launched and gave as output the report file with the processed and sorted data.
In particular, this report file is an excel file. Other than some standard information about the turbine, such as vibe survey engine, name of the engine in which the componenet is used, whether the turbine is LPT or HPT, each row of this excel file contains a pair of data relating to a measurement (speed [rpm] and frequency [Hz]) to which the following information is associated:

- stage of the turbine for that pair of data;
- code of the strain gauge that got the measure;
- magnitude of the forced response [miscrostrn p2p];
- EO;

An example is shown in table 4.1 [2].
Speed, frequency and magnitude of the response are necessary to plot the Campbell diagram. The other information are used to make the dashboard more interactive and

[2]Numbers and name are all invented

user friendly.

LPT/HPT	Engine	Stage	Accel/Decel	Vibe survey engine	S/G type	S/G code	Speed [rpm]	Frequency [Hz]	Magnitude [microstrn p2p]	EO
LPT	enigine name	S1V	Acc	vibe survey code	SG1	ABC00	100	3	15	20

Table 4.1: Example of a row of the report file.

4.1.2 Dashboard

As previously written, the dashboard is a Avio Aero corporate Spotfire tool.
It contains information about several turbines of GE engines. In particular, data regarding experimental test with the aim of measuring the forced response of the turbines is collected.
This tool is very important because it greatly supports designers in the design phase of new components: in fact, if a turbine has to be designed with characteristics similar to an existing one, it is possible to immediately notice what the criticalities may be and therefore try to avoid them thanks to the information contained in the Dashboard.
This Dashboard is composed by several panels. Each of them is dedicated to a turbine and is linked with the post processed data of the related experimental test, contained in the report file that comes from the *postpro tool*.
The work carried out in this thesis was to generate a panel to be dedicated to a turbine of a GE program that had not yet been inserted in the Dashboard and correctly set all the information obtained in the previous steps. Indeed, other than data of the report file, also other information needs to be inserted, such as:

- the number of stages;
- the airfoil count of each blade/vane;
- the material of each blade/vane;

- the location of strain gauges;
- etc.

For reasons of corporate secrecy, the generated Dashboard cannot be shown and published in this thesis. For this reason it has been generated another panel in which ***both names and data were invented*** as example to better explain how the Dashboard works.

Example Initally, a Dashboard panel appears as shown in figure 4.3. It is possible to see the cross section of the turbine, but all the plots and the table are empty because no stage has been selected yet.

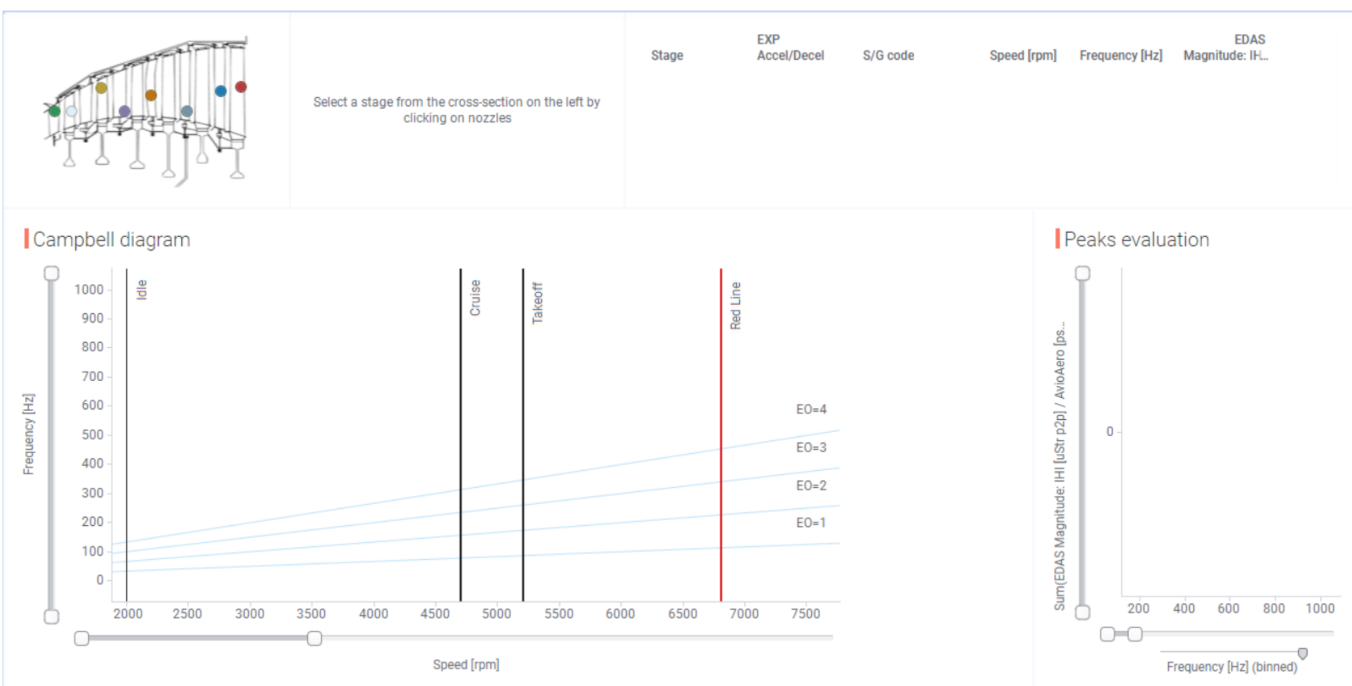

Figure 4.3: Example of Dashboard panel.

We can see that it is written: *"Select a stage from the cross-section on the left by clicking on nozzles"*. So, from the cross section it is possible to select one of the stage (and also choose blade or vane). Let's choose for example the first one, which is the IGVS (fig 4.4, colored in dark green).

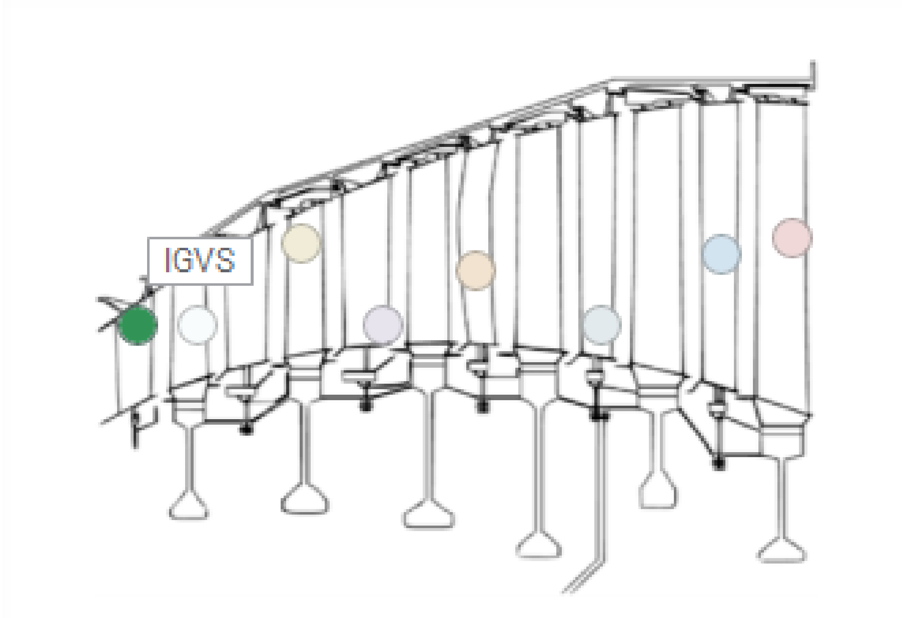

Figure 4.4: Selection of the first stage in the cross section of the turbine.

After the selection of the stage the panel will appear as shown in figure 4.5.

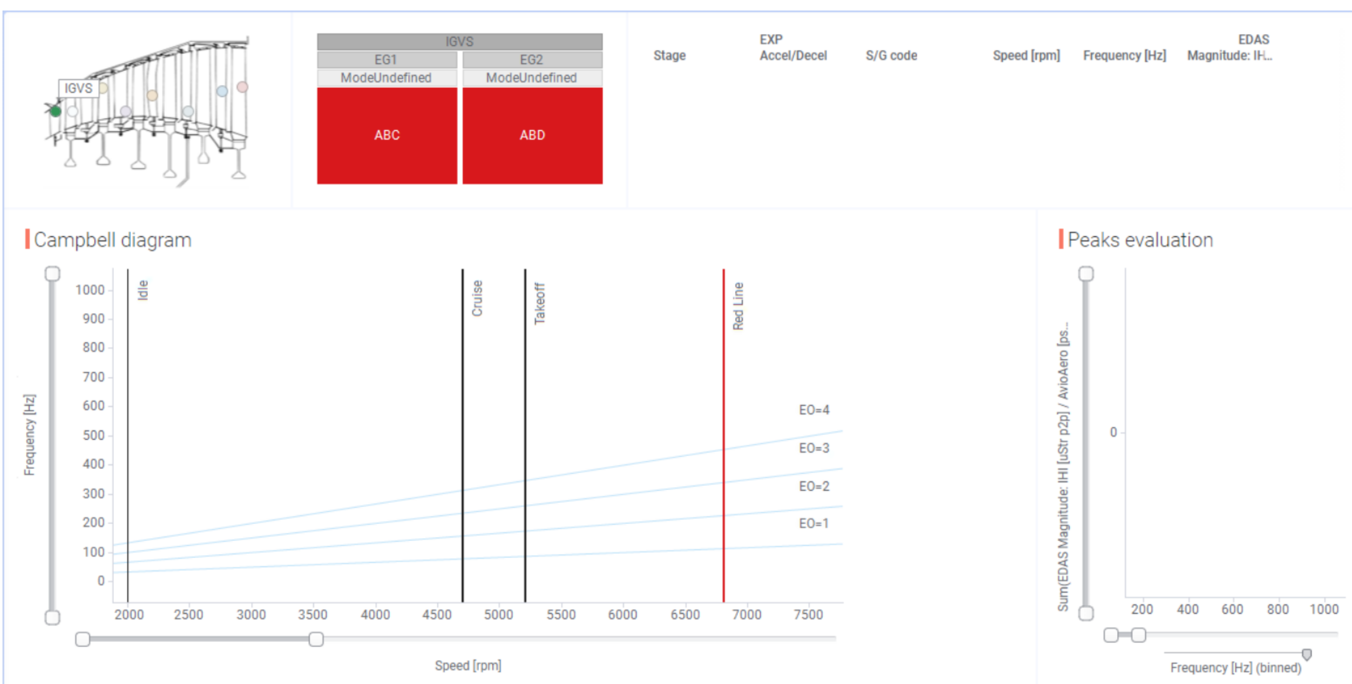

Figure 4.5: Dashboard panel after stage selection.

We can see that there is no more writing, but there is another selection menu from which we need to select a strain gauge code. Each code is related to the measure that the strain gauge obtained during the test [3] (fig 4.6).

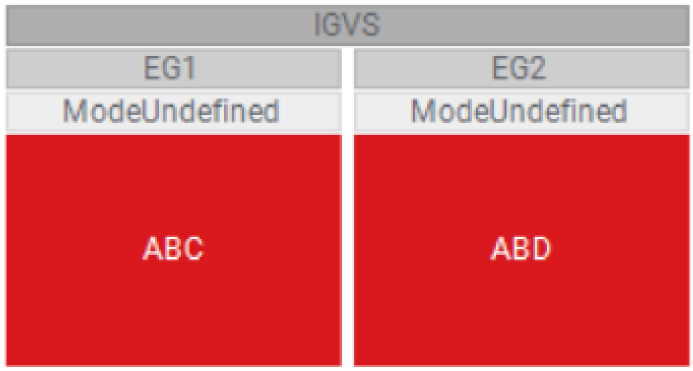

Figure 4.6: Strain gauges selection.

Let's choose for example the strain gauge *ABC*. After the selection of the strain guage, the panel will appear as shown in figure 4.7.

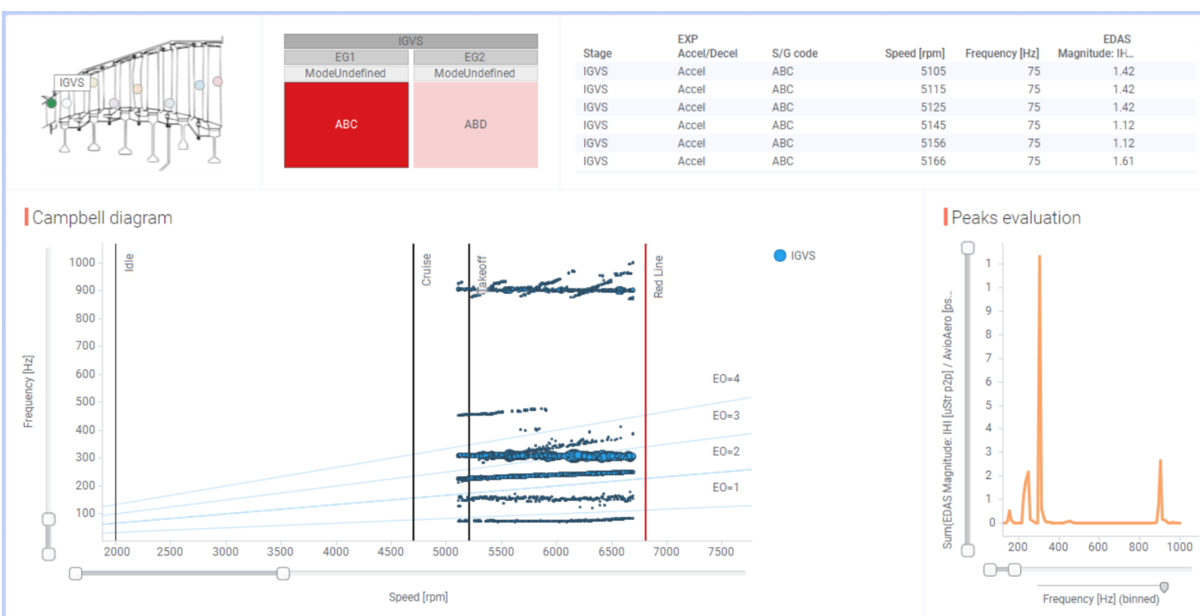

Figure 4.7: Dashboard panel after strain gauge selection.

[3]For this invented example only two strain gauges were inserted but there can be more of them for a single stage

So now the diagrams and the table are no more empty. In particular, the Dashboard contents are:

- the Campbell diagram (fig 4.8), in which it is possible to evaluate the forced response of the selected stage;
- a table (fig 4.9) in which the values of the Campbell diagram are reported;
- a plot (fig 4.10) for the evaluation of peak regarding forced response.

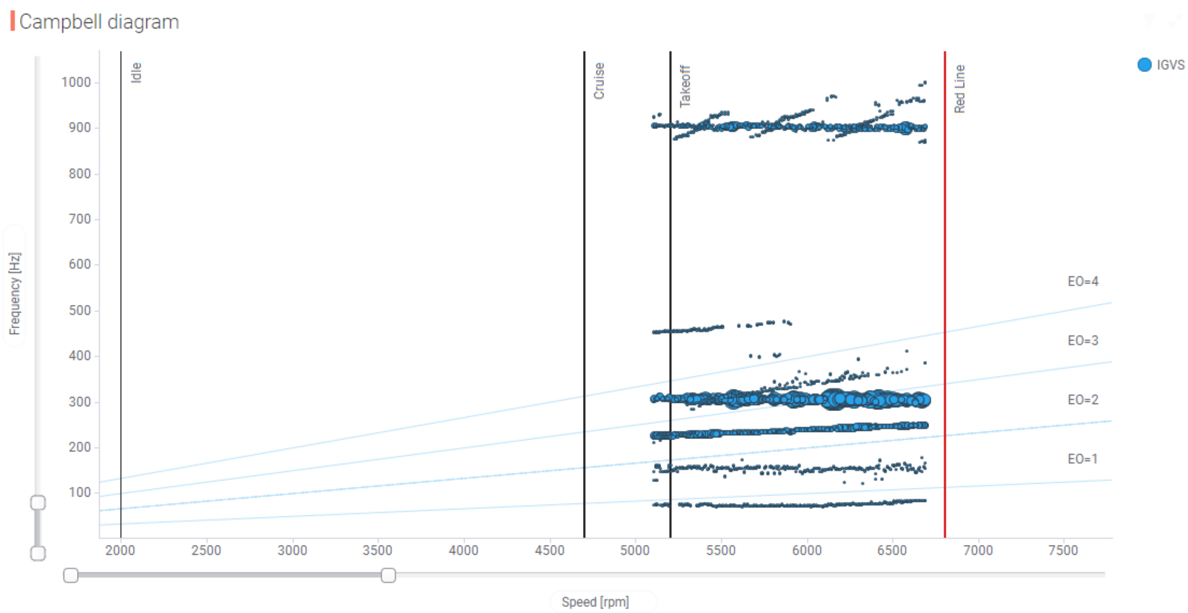

Figure 4.8: Campbell diagram.

Stage	EXP Accel/Decel	S/G code	Speed [rpm]	Frequency [Hz]	EDAS Magnitude: IH...
IGVS	Accel	ABC	5105	75	1.42
IGVS	Accel	ABC	5115	75	1.42
IGVS	Accel	ABC	5125	75	1.42
IGVS	Accel	ABC	5145	75	1.12
IGVS	Accel	ABC	5156	75	1.12
IGVS	Accel	ABC	5166	75	1.61
IGVS	Accel	ABC	5176	75	1.61
IGVS	Accel	ABC	5186	75	1.61
IGVS	Accel	ABC	5196	72	1.03

Figure 4.9: Table of values.

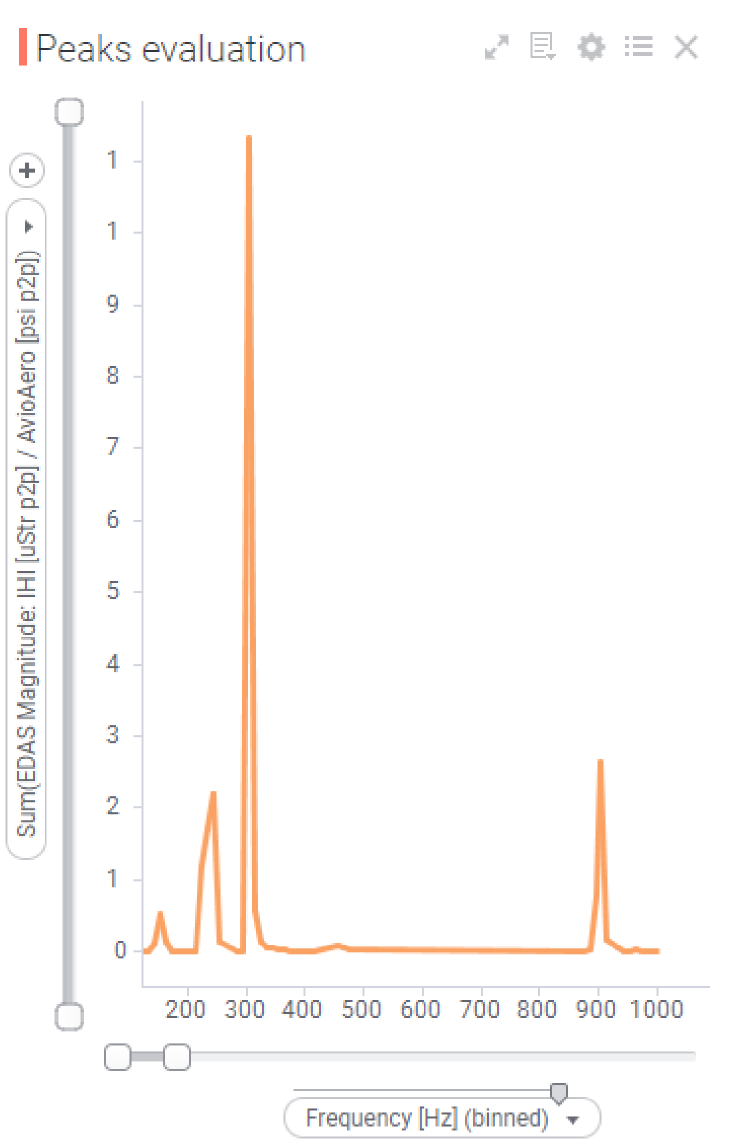

Figure 4.10: Peak evaluation.

Chapter 5

Conclusions and future developments

All of the work done on this thesis will be replicated in this last chapter. In particular, the steps carried out in the previous chapters will be summarized, then the results obtained will be reported and then some possible future developments will be presented.
The introduction (chapter 1) of this thesis deal with theoretical notions about aero engines and then LPT other than some aspects about E-TDCs and ARIAS project.
The main topic of this thesis is the optimization of processes related to modal analysis of bladed disks. For this reason, in chapter 2 some general concepts have been introduced to explain the dynamics of bladed disks, focusing on aspects such as the meaning of modal analysis, cyclic symmetry, harmonic indices etc. Furthermore, the phenomena of forced response and aeromechanical instabilities concerning bladed disks were exposed.
On the other hand chapters 3 and 4 represent the main core of the thesis, in which all the work done has been exposed. The main topics can be subdivided into the following three macro categories:

- Best mesh order for modal analysis;
- Optimized post processing activities;

- Test data collection.

For each of these categories a paragraph will be dedicated for the conclusions.

Best mesh order for modal analysis

The first optimization study was a sensitivity study to understand which mesh was most suitable to perform a modal analysis. Considering the ARIAS bladed disk, two fem models have been generated:

- **model A**, with first-order hexa and second order tetra, so less accurate but also less computationally heavy (fig. 5.1(a));
- **model B**, with both hexa and tetra of second order, therefore more accurate but also heavier on a computational level (fig. 5.1(b)).

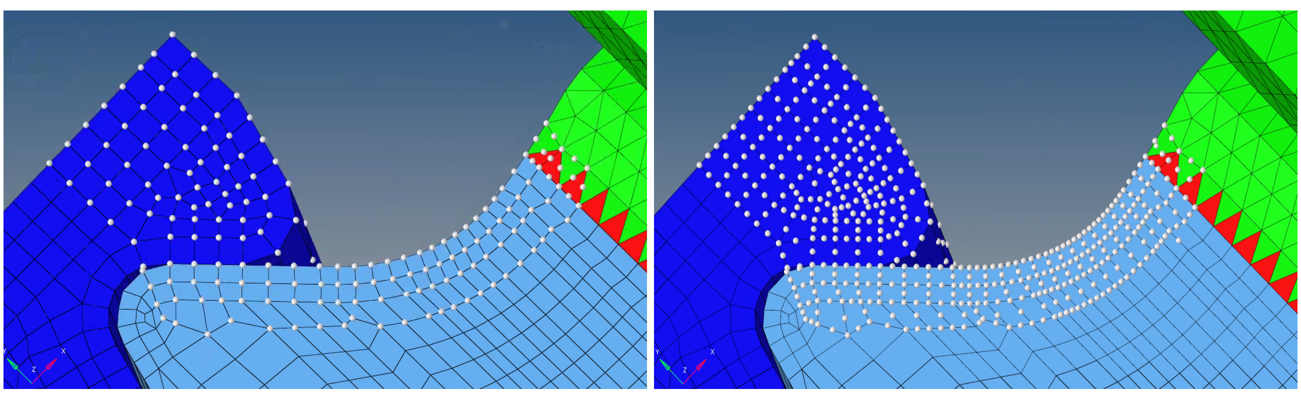

(a) Model A. (b) Model B.

Figure 5.1: Difference between the two models.

For both these models the same modal prestressed analysis has been performed. The main characteristics and the time that the anlyses last are exposed in the following table 5.1.

	Model A	Model B
Number of elements	782692	782692
Number of nodes	1115285	1499689
HEXA	FIRST ORDER	SECOND ORDER
TETRA	SECOND ORDER	SECOND ORDER
CPU time to perform the analysis	$11h$	$21h$

Table 5.1: Summary of the characteristics and analysis times for the two models.

The results are shown in the following table 5.2.

MODE	Harmonic Index	$f_A[Hz]$	$f_B[Hz]$	$\frac{\lvert f_A - f_B \rvert}{f_A}[\%]$	MAC
1	1	205.10	204.16	0.4583	1.0000
1	36	206.53	205.94	0.2857	1.0000
1	71	206.29	205.71	0.2812	1.0000
1	1	451.57	440.45	2.4625	0.9998
1	36	529.73	529.01	0.1359	1.0000
1	71	532.87	532.15	0.1351	1.0000
1	1	4239.9	4225.6	0.3373	0.9998
1	36	5552.0	5548.4	0.0648	1.0000
1	71	5572.1	5568.4	0.0664	1.0000

Table 5.2: Comparison of results.

In conclusion, the best model to perform this kind of analysis is model A because it produces same model B results but in shorter time (50%), i.e. there is a negligible impact of HEXA 2^{nd} order elements.

Optimized post processing activities

There are numerous post processing activities that must be completed to process the results of a modal analysis. Some of these have been taken into account with the intention of simplifying the process and accelerating execution times.
These activities are:

- modal shape recognition (see tab. 5.3);
- FreND generation (process simplified);
- generation of report file for flutter analysis (see tab. 5.4).

For each aspect it has been designed some specific APDL macros to improve the processes. The results are shown in the following tables.

	Current	Optimize - Step 1	Optimize - Step 2 (cluster)
Time reduction	-	77%	70%
Other activities in parallel	no	no	yes
Enable 360° plot	no	no	yes

Table 5.3: Advantages obtained as for modal shape recognition.

	Current	Optimize - Step 1	Optimize - Step 2 (cluster)
Time reduction	-	43%	95%
Other activities in parallel	no	no	yes

Table 5.4: Advantages obtained as for the generation of report files for flutter analysis.

Test data collection

As for test data collection, the aim was to create a new panel in the corporate Dashboard in which inserting new data about a LPT of a GE program. In addition to create the panel, it was necessary to process the data from the experimental tests and search for information on the turbine in the related report.
All these things were done succesfully and the new panel with all the information has been created. This, together with the other panels, will support the designers in the design phase of new turbines.

Future developments

There are several other aspects of post processing that can be improved through the design of new APDL macros. An example can be the automatic creation of videos containing animations of the modal shapes, to make the recognition of the modal shapes themselves even easier.
Besides, another example could be to add functionality to the 'flutter converter' tool so that it can generate files necessary for the forced response (similar to those necessary for flutter analyses).
As for the last part, a possible improvement could be to add as many turbines as possible to the Dashboard, in order to increase the data contained in the database.

List of Figures

List of Tables

Bibliography

[1] Rolls Royce, *The jet engine*, Renault Printing Co Ltd, Birmingham, Fifth edition, 1996.

[2] Michelangelo Flaccavento, *Motori aeronautici*, Hoelphi, Trento, , 2016.

[3] Jack D. Mattingly, *Elements of propulsion : Gas Turbines and Rockets*, American Institute of Aeronautics and Astronautics, 2000. ProQuest Ebook Central, https://ebookcentral.proquest.com/lib/polito-ebooks/detail.action?docID=3111475.

[4] Jack D. Mattingly, William H. Heiser, David T. Pratt, *Aircraft Engine Design*, American Institute of Aeronautics and Astronautics, 2000. ProQuest Ebook Central, https://ebookcentral.proquest.com/lib/polito-ebooks/detail.action?docID=3111670.

[5] Stefano Zucca, *Dinamica dei Rotori per Applicazioni Aerospaziali*, Dipartimento di Ingegneria Meccanica e Aerospaziale, Politecnico di Torino, , inedito, 2021.

[6] Marco Gherlone, *Strutture Aeronautiche*, Dipartimento di Ingegneria Meccanica e Aerospaziale, Politecnico di Torino, , inedito, 2021.

[7] Roberto Marsilio, *Progetto di Motori per Aeromobili*, Dipartimento di Ingegneria Meccanica e Aerospaziale, Politecnico di Torino, , inedito, 2021.

[8] Marco Petrolo, *Aeroelasticità*, Dipartimento di Ingegneria Meccanica e Aerospaziale, Politecnico di Torino, , inedito, 2021.

[9] Valerio Piscopo, *Analysis of Mulstistage Structures using Cyclic Symmetry*, MSc thesis, Dipartimento di Ingegneria Meccanica e Aerospaziale, Politecnico di Torino, 2022.

[10] Alberto Civardi, *Development and Validation of Algorithms for Vibration Monitoring of Aeronautical Engines*, MSc thesis, Dipartimento di Ingegneria Meccanica e Aerospaziale, Politecnico di Torino, 2020.

[11] Valeria Pinto, *Aeromechanical Optimization of Aeronautical Low Pressure Turbine Components*, PhD thesis, Dipartimento di Ingegneria Meccanica e Aerospaziale, Politecnico di Torino, 2020.

[12] Matteo Nicita, *Extraction of relevant data from experimental test and matching with FEA*, MSc thesis, Dipartimento di Ingegneria Meccanica e Aerospaziale, Politecnico di Torino, 2022.

[13] Andrea Ciriello, *Airfoils Clashing Technology for Turbofan LPT Overspeed Prevention*, MSc thesis, Dipartimento di Ingegneria Meccanica e Aerospaziale, Politecnico di Torino, 2022.

[14] *Arias Project*, URL: `https://www.arias-project.eu/`, [Last access 22/02/2023].

[15] *Newton-s Third Law*, URL: `hhttps://www.grc.nasa.gov/www/BGH/newton3.html`, [Last access 22/02/2023].

[16] *Chapter 10: Multipoint Constraints and Assemblies*, URL: https://ansyshelp.ansys.com/account/secured?returnurl=/Views/Secured/corp/v222/en/ansctec/Hlpctecmpcassm.html?q=MPC, [Last access 22/02/2023].

[17] *ANSYS Contact Technology Guide*, URL: https://www.cae.tntech.edu/chriswilson/FEA/ANSYS/gctec90.pdf, [Last access 22/02/2023].

[18] *Altair Hypermesh*, URL: https://www.altair.com/hypermesh, [Last access 22/02/2023].

[19] *UE actions to reduce emission of aircrafts*, URL: https://www.europarl.europa.eu/news/it/headlines/society/20220610STO32720/azioni-dell-ue-per-ridurre-le-emissioni-di-navi-e-aerei#::text=Al%20fine%20di%20ridurre%20le,emissioni%20in%20entrambi%20i%20settori., [Last access 21/03/2023].

[20] Miroslav Pastor, Michal Binda, Tomáš Harčarik, *Modal Assurance Criterion*,In: *Procedia Engineering* 48, 2012.

[21] Srinivasan A.V., *Flutter and Resonant Vibration Characteristics of Engine Blades*, Journal of Engineering for Gas Turbines and Power, 1997.

FIGURES

[22] Figure 1.3, *Newton-s Third Law* [15].

[23] Figure 1.4, https://it.wikipedia.org/wiki/CiclodiBrayton-Joule#/media/File:BraytonpvTs.svg.

[24] Figure 1.5, https://commons.wikimedia.org/wiki/File:Jetenginenumbered.svg.

[25] Figure 1.6, https://commons.wikimedia.org/wiki/File:Turbojetoperation-axialflow.png.

[26] Figure 1.7, http://aviationknowledge.wikidot.com/aviation:jet-aircraft.

[27] Figure 1.8, https://upload.wikimedia.org/wikipedia/commons/7/75/Turbofanoperation.svg.

[28] Figure 1.9, https://www.boeing.com/commercial/aeromagazine/articles/2012q3/2/.

[29] Figure 1.10 (a), *Analysis of Mulstistage Structures using Cyclic Symmetry* [9].

[30] Figure 1.10 (b), https://commons.wikimedia.org/wiki/File:Velocity-triangles-kk-20050824.png.

[31] Figure 1.11, `https://d2t1xqejof9utc.cloudfront.net/screenshots/pics/34552b299a1ace1777baeda550d1fdb7/large.jpg`.

[32] Figure 1.12, `https://journals.sagepub.com/doi/10.1177/0954410017728972`.

[33] Figure 2.1 (a), *Dinamica dei Rotori per Applicazioni Aerospaziali* [5].

[34] Figure 2.2 (a), *Dinamica dei Rotori per Applicazioni Aerospaziali* [5].

[35] Figure 2.3 (a), *Dinamica dei Rotori per Applicazioni Aerospaziali* [5].

[36] Figure 2.5 (a), *Analysis of Mulstistage Structures using Cyclic Symmetry* [9].

[37] Figure 2.6 (a), *Analysis of Mulstistage Structures using Cyclic Symmetry* [9].

[38] Figure 2.7 (a), *Dinamica dei Rotori per Applicazioni Aerospaziali* [5].

[39] Figure 2.7 (b), *Dinamica dei Rotori per Applicazioni Aerospaziali* [5].

[40] Figure 2.9 (b), *Aeromechanical Optimization of Aeronautical Low Pressure Turbine Components* [11].

[41] Figure 2.10 (b), *Aeromechanical Optimization of Aeronautical Low Pressure Turbine Components* [11].

[42] Figure 2.11 (b), *Aeromechanical Optimization of Aeronautical Low Pressure Turbine Components* [11].

[43] Figure 2.12 (b), *Aeromechanical Optimization of Aeronautical Low Pressure Turbine Components* [11].

[44] Figure 2.13 (b), *Extraction of relevant data from experimental test and matching with FEA* [12].

[45] Figure 1.13 (b), *Arias Project* [14].

[46] Figure 1.14 (b), *Arias Project* [14].

[47] Figure 2.4 (b), *Dinamica dei Rotori per Applicazioni Aerospaziali* [5].

[48] Figure 2.4 (b), *Dinamica dei Rotori per Applicazioni Aerospaziali* [5].

[49] Figure 2.4 (b), *Dinamica dei Rotori per Applicazioni Aerospaziali* [5].